

# High-Z-Sensitized Radiotherapy Synergizes with the Intervention of the Pentose Phosphate Pathway for In Situ Tumor Vaccination

Yuxiang Wang, Jing Chen, Rumeng Duan, Rong Gu, Weiran Wang, Jinhui Wu, Huibo Lian,\* Yiqiao Hu,\* and Ahu Yuan\*

In situ tumor vaccination is preliminarily pursued to strengthen antitumor immune response. Immunogenic tumor cell death spontaneously releases abundant antigens and adjuvants for activation of dendritic cells, providing a paragon opportunity for establishing efficient in situ vaccination. Herein, Phy@PLGdH nanosheets are constructed by integrating physcion (Phy, an inhibitor of the pentose phosphate pathway (PPP)) with layered gadolinium hydroxide (PLGdH) nanosheets to boost radiation-therapy (RT)-induced immunogenic cell death (ICD) for potent in situ tumor vaccination. It is first observed that sheet-like PLGdH can present superior X-ray deposition and tumor penetrability, exhibiting improved radiosensitization in vitro and in vivo. Moreover, the destruction of cellular nicotinamide adenine dinucleotide phosphate (NADPH) and nucleotide homeostasis by Phy-mediated PPP intervention can further amplify PLGdH-sensitized RT-mediated oxidative stress and DNA damage, which correspondingly results in effective ICD and enhance the immunogenicity of irradiated tumor cells. Consequently, Phy@PLGdH-sensitized RT successfully primes robust CD8<sup>+</sup>-T-cell-dependent antitumor immunity to potentiate checkpoint blockade immunotherapies against primary and metastatic tumors.

antitumor immune response against primary and metastatic tumors.<sup>[2]</sup> Different from conventional vaccines, in situ vaccination could conveniently convert established tumors into a “vaccine factory” to release various tumor antigens for stimulating and diversifying antitumor T-cell response.<sup>[3]</sup> Radiation therapy (RT) is a widely used local therapy of malignancies and exhibits great potential in inducing in situ tumor vaccine effect.<sup>[4]</sup> However, even potentiated by CBI, RT could only lead to mild to moderate immune response within nonirradiated tumors, which is far less than medical needs.<sup>[5]</sup> Therefore, it is quite meaningful to boost RT-mediated in situ vaccination to extend its therapeutic effect to the whole body.

To achieve this goal, a possible way could be potentiating RT-induced immunogenic cell death (ICD). ICD is a death modality accompanied by releasing tumor antigens and damage-associated molecular patterns, including calreticulin

## 1. Introduction

Successful antitumor immune priming effectively guarantees the therapeutic efficacy of current immunotherapies, especially for checkpoint blockade immunotherapies (CBIs,  $\alpha$ PD-1,  $\alpha$ PD-L1, or  $\alpha$ CTLA4).<sup>[1]</sup> In situ tumor vaccination seeks to enhance the immunogenicity of tumor cells and prime systemic

(CRT), high mobility group protein B1 (HMGB1), etc., which could provide antigens and adjuvants for tumor vaccination.<sup>[6]</sup> Currently, some studies have indicated that oxidative stress and DNA damage within tumor cells could potentially result in ICD.<sup>[7]</sup> However, due to the insufficient deposition of X-ray within tumor tissues, only low level of reactive oxygen species (ROS) could be produced to induce oxidative stress upon the recommended radiation doses. To address this problem, radiosensitizers based on high-Z elements are being developed widely to deposit X-ray for amplifying RT-induced oxidative stress. Of note, HfO<sub>2</sub> nanoparticles (Hensify) have been approved in Europe for locally advanced soft tissue sarcoma treatment<sup>[8]</sup> and are confirmed to augment RT-mediated antitumor immunity effect in many clinical trials. However, their slight improvements suggest the room for optimization.<sup>[9]</sup>

The pentose phosphate pathway (PPP) is a branch of glycolysis and hyperactive in most tumors,<sup>[10]</sup> which could provide abundant NADPH and ribose 5-phosphate to maintain redox and nucleotides homeostasis, respectively.<sup>[11]</sup> NADPH is a central player in cellular antioxidant system, which not only mediates GSH synthesis,<sup>[12]</sup> but also acts as an electron donor to reduce oxidized GSH and thioredoxin (Trx, an important

Y. Wang, J. Chen, R. Duan, R. Gu, W. Wang, J. Wu, Y. Hu, A. Yuan  
State Key Laboratory of Pharmaceutical Biotechnology  
Medical School and School of Life Science  
and Jiangsu Key Laboratory for Nano Technology  
Nanjing University  
Nanjing 210093, China  
E-mail: huyiqiao@nju.edu.cn; yuannju@nju.edu.cn

H. Lian  
Department of Urology  
Zhejiang Provincial People's Hospital  
Hangzhou, Zhejiang 310014, China  
E-mail: lianhuibo@hmc.edu.cn

 The ORCID identification number(s) for the author(s) of this article can be found under <https://doi.org/10.1002/adma.202109726>.

DOI: 10.1002/adma.202109726

oxidoreductase).<sup>[13]</sup> Many studies have revealed that eliminating NADPH by inactivating glucose-6-phosphate dehydrogenase (G6PD) or 6-phosphogluconate dehydrogenase (6PGD), the rate-limiting enzymes in PPP, could sensitize tumor cells to oxidative stress.<sup>[14]</sup> As another product of PPP, ribose 5-phosphate is the precursor of nucleotides, closely participating in DNA damage repair.<sup>[15]</sup> This evidence indicates that PPP is potentially essential for tumor cell survival upon RT by alleviating RT-induced oxidative stress and DNA damage, which correspondingly impede RT-induced ICD. Thus, we suppose that the combination of high-Z-sensitized RT and PPP intervention would induce potent vaccine effects to bolster antitumor immunity by inducing strong ICD.

To augment X-ray deposition of tumor tissues, the poly(ethylene glycol) (PEG)-modified layered gadolinium hydroxide (PLGdH) nanosheets based on gadolinium (Gd, high-Z element, widely used in magnetic resonance imaging (MRI) in the clinic) were involved in our study. We were surprised to find that sheet-like PLGdH could exhibit more pronounced X-ray deposition for ROS generation when compared to spherical Gd-based nanoscale coordinate polymers (Gd-NCPs, prepared in our previous work), probably attributed to their larger water-accessible surface areas. Meanwhile, the sheet-like structure could also confer PLGdH better tumor penetrability, leading to the improved radiotherapeutic effects for tumor tissues away from the blood vessels. To intervene the PPP, physcion (Phy, an anion inhibitor of 6PGD screened from drugs approved by the US Food and Drug Administration (FDA)) was exchanged into the interval of PLGdH to form Phy@PLGdH nanosheets. Our results showed that owing to the destruction of cellular NADPH and nucleotide homeostasis, obtained Phy@PLGdH nanosheets further amplified PLGdH-sensitized RT-induced oxidative stress and DNA damage, then effectively suppressed the growth of primary tumors. Meanwhile, this damage to tumor cells triggered strong ICD with

the drastic exposure or release of CRT, HMGB1, and adenosine triphosphate (ATP), respectively. More importantly, the delay of DNA repair process, caused by the PPP intervention, potentially increased the leakage of DNA fragments, and promoted the secretion of IFN- $\beta$  from neighboring immune cells for further reversing the immunosuppressive tumor microenvironment (TME). Then, Phy@PLGdH-sensitized radiation therapy primed robust CD8<sup>+</sup>-T-cell-dependent antitumor immunity and significantly potentiated  $\alpha$ PD-L1 checkpoint blockade immunotherapy. In summary, we have developed Phy@PLGdH nanosheets for synergistically improving RT-induced ICD, which yielded robust in situ vaccination to inhibit primary and metastatic tumors (Figure 1).

## 2. Results

### 2.1. Preparation and Characterization of Phy@PLGdH Nanosheets

The layered gadolinium hydroxides (LGdHs), [Gd<sub>2</sub>(OH)<sub>5</sub>(H<sub>2</sub>O)<sub>x</sub>]Cl, were synthesized by hydrothermal reaction in the Gd<sup>3+</sup>-containing alkaline aqueous solution.<sup>[16]</sup> Then, sodium oleate was inserted into interlayer space of LGdH in H<sub>2</sub>O, which could be readily delaminated in nonpolar organic solvent (such as CHCl<sub>3</sub>) to generate oleic acid-modified LGdH (OA-LGdH) nanosheets. To provide LGdH with water compatibility, film dispersed PEG-DSPE was used to modify OA-LGdH and then PEGylated LGdH nanosheets were obtained.<sup>[17]</sup> To integrate 6PGD inhibitor Phy into nanosheets, Phy was first exchanged into interlayer spaces of OA-LGdH in CH<sub>2</sub>Cl and then modified with DSPE-PEG to obtain physcion-encapsulated PLGdH (Phy@PLGdH) nanosheets (Figure 2a). As shown in Figure 2b and Figure S1 (Supporting Information), the ultra-high-resolution field emission scanning electron microscope

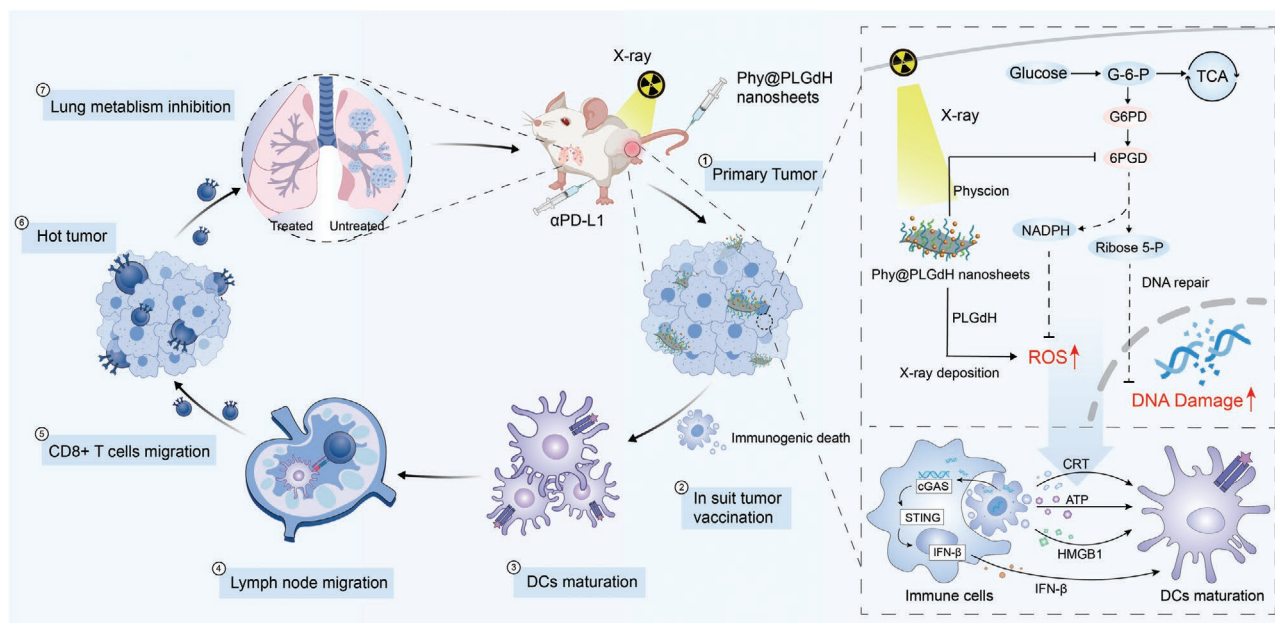
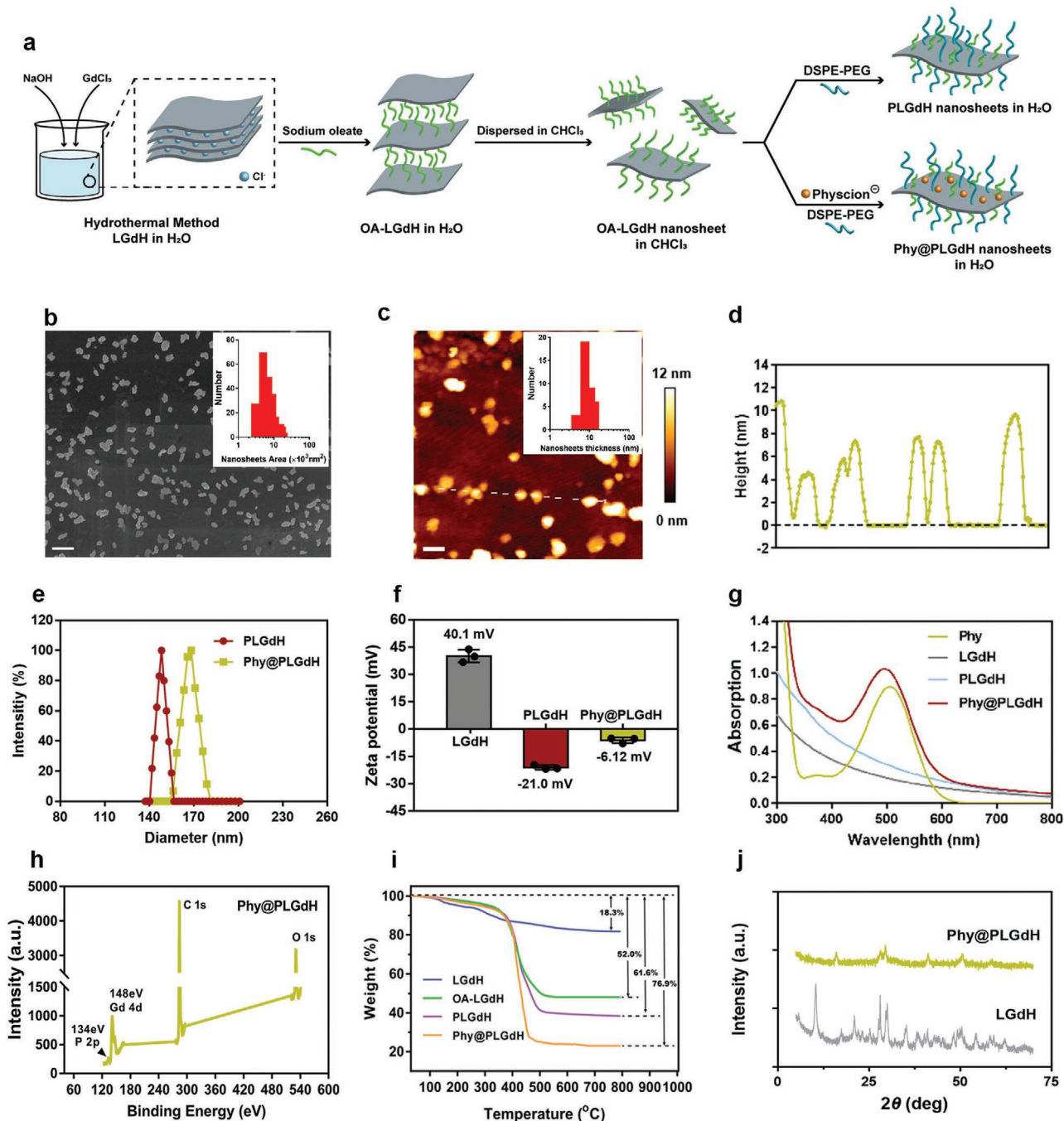


Figure 1. Phy@PLGdH nanosheets promoted radiation-induced in situ tumor vaccination.



**Figure 2.** Preparation and characterization of Phy@PLGdH nanosheets. a) Schematic diagram of Phy@PLGdH preparation process. b) Ultrahigh-resolution field-emission scanning electron microscopy (FE-SEM) imaging of Phy@PLGdH nanosheets. Inset: histogram of area distribution of Phy@PLGdH nanosheets. Scale bar = 400 nm. c) Atomic force microscopy (AFM) images of Phy@PLGdH nanosheets. Scale bar = 200 nm. Inset: histogram of thickness distribution of Phy@PLGdH nanosheets. d) Height profiles along the white lines in (c). e) Average hydrodynamic sizes of PLGdH, Phy@PLGdH nanosheets. f) Zeta potential of LGdH, PLGdH, Phy@PLGdH nanosheets. Data are shown as mean  $\pm$  standard deviation (SD),  $n = 3$ . g) Normalized UV-vis spectra of phycion, LGdH, PLGdH, or Phy@PLGdH. h) Element analysis of Phy@PLGdH nanosheets by X-ray photoelectron spectroscopy (XPS). i) The thermogravimetric curves of LGdH, OA-LGdH, PLGdH, and Phy@PLGdH between 30 and 800 °C. j) PXRD patterns of Phy@PLGdH nanosheets.

(FE-SEM) images of Phy@PLGdH and PLGdH indicated their irregular shapes. The average lateral size and area of the observed Phy@PLGdH were 158.8 nm and 6803.6 nm<sup>2</sup>, respectively, which were both calculated by Image J (Figure 2b).

Then, the thickness of Phy@PLGdH determined by atomic force microscopy (AFM) (Figure 2c,d) was ranged from 4.5 to 13.8 nm, with the average thickness of 8.6 nm. These results indicated that Phy@PLGdH nanosheets were slightly thicker

than PLGdH nanosheets (about 4.3 nm, Figure S2, Supporting Information), potentially induced by physcion loading. Dynamic light scattering (DLS) showed that the average hydrodynamic diameter of PLGdH and Phy@PLGdH nanosheets were about 148.3 and 168.4 nm, respectively (Figure 2e). As shown in Figure 2f, LGdHs exhibited positive surface charges due to their composition of metal hydroxide. After delaminated with OA and modified with DSPE-PEG, the zeta potential of PLGdH and Phy@PLGdH decreased to  $-21.0$  and  $-6.1$  mV, respectively. Then, UV-vis analysis suggested that Phy@PLGdH nanosheets and free physcion had similar absorption peaks at about 507 nm, whereas no absorption peak could be observed in LGdH and PLGdH, demonstrating the presence of Phy within Phy@PLGdH nanosheets (Figure 2g). Moreover, the molar ratio of Gd and Phy in the established nanosheets was quantitatively determined to be 4:1. Meanwhile, X-ray photoelectron spectroscopy (XPS) indicated that P, C, O, Gd elements could be observed in Phy@PLGdH nanosheets with the molar ratio of Gd to P (from DSPE-PEG) of 46.5:1 (Figure 2h and Figure S3 (Supporting Information)). To further confirm the composition of Phy@PLGdH nanosheets, we performed the thermogravimetric analysis (TGA). The thermogravimetric curves (Figure 2i) showed that the weight loss of LGdH, OA-LGdH, PLGdH, and Phy@PLGdH during 30–800 °C were 18.3%, 52.0%, 61.6%, and 76.9%, which indicated that the weight percentage of LGdH, OA, PEG, and Phy within Phy@PLGdH was  $\approx 42.8\%$ , 24.2%, 8.15%, and 15.3%, respectively. These TGA results indicated that the molar ratio of Gd, Phy, and PEG-DSPE was  $\approx 3.9:1:0.08$ , which was roughly consistent with the results from XPS and quantitative methods. Therefore,

we finally confirmed the existence of Gd, Phy, DSPE-PEG in Phy@PLGdH nanosheets, and their molar ratio was identified as 4:1:0.08. The crystal forms of LGdH and Phy@PLGdH were assessed by powder X-ray diffraction (PXRD), presenting some similar strong (00l) reflections and indicating that the structure of LGdH could be maintained after PEGylation and physcion loading (Figure 2j).

We next assessed the functional characteristics of Phy@PLGdH nanosheets (Figure 3a). As shown in Figure 3b,c, the modification of LGdH by OA and DSPE-PEG exhibited more excellent acid stability than LGdH. At pH 4.0, 5.0, and 6.0, about 86.0%, 35.6%, and 3.4% Gd<sup>3+</sup> were released from LGdH within 24 h, respectively. Alternatively, PLGdH showed almost no degradation at pH = 6.0 or 5.0. Even at pH = 4.0, PLGdH only exhibited less than 20% dissolution within 24 h. Furthermore, PLGdH and Phy@PLGdH nanosheets exhibited greater stability than LGdH in 50% fetal bovine serum (FBS) at 37 °C (Figure 3d). The autocorrelation curve of LGdH dispersed in 50% FBS indicated that their movements did not follow the law of Brownian motion, potentially revealing their obvious aggregation (Figure S4, Supporting Information). To mimic the in vivo biostability and drug release capability, we examined the release profiles of Phy from Phy@PLGdH nanosheets under different pH conditions. As shown in Figure S5 (Supporting Information), when at pH 7.4, less than 10% Phy released from Phy@PLGdH within 24 h, potentially indicating their biostability during blood circulation. When pH decreased to 6.0 and 5.0, there were about 38.2% and 50.2% physcion that could be released from Phy@PLGdH. These pH-dependent release profiles might be related to the protonation of physcion molecules

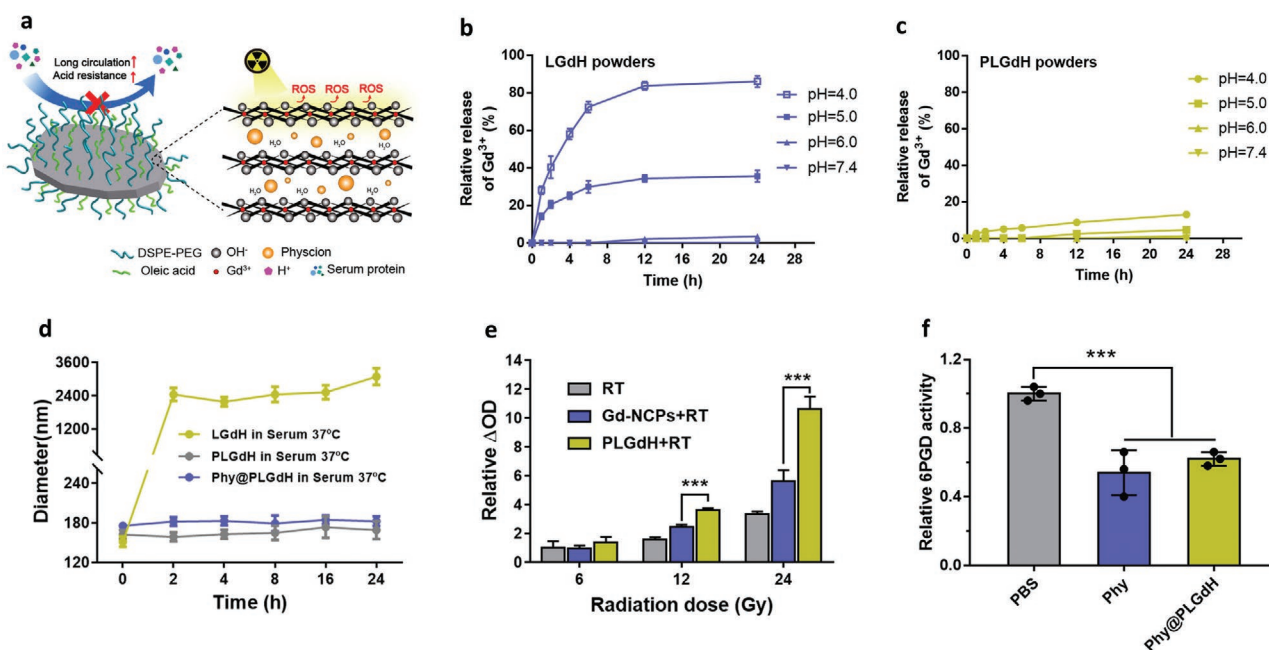


**Figure 3.** Functional characterization of Phy@PLGdH nanosheets. a) Schematic microstructure of Phy@PLGdH nanosheets. b,c) Time-dependent relative Gd<sup>3+</sup> release from LGdH (b) and PLGdH (c) in pH 4.0–7.4 buffer solutions. Data are shown as mean  $\pm$  SD,  $n = 3$ . d) The change of particle size of LGdH, PLGdH, Phy@PLGdH in 50% fetal bovine serum (FBS) at 37 °C, respectively. Data are shown as mean  $\pm$  SD,  $n = 3$ . e) ROS generation measured by methylene blue (MB) degradation during RT at different doses. Data are shown as mean  $\pm$  SD ( $n = 3$ , one-way ANOVA). f) Cellular 6PGD inhibition of free physcion and Phy@PLGdH nanosheets. Data are shown as mean  $\pm$  SD ( $n = 3$ , one-way ANOVA). N.S. represents nonsignificance, and \*\*\* $p < 0.001$ .

under weak acidic conditions (e.g., tumor microenvironment or cellular lysosomes), which highly weaken the adsorption capacity between physcion and PLGdH nanosheets. Then, we evaluated the ability of PLGdH in enhancing RT-mediated ROS generation via methylene blue (MB) bleaching method. As shown in Figure 3e, PLGdH+RT bleaching MB more efficient than RT alone in a dose-dependent manner, indicating that Gd ion within PLGdH could improve X-ray deposition for more ROS generation. To explore whether nanosheets have superiority in depositing X-ray, we introduced the previously established spherical-nanoscale-coordinated-nanoparticles-based Gd for comparison. Interestingly, PLGdH-nanosheet-sensitized radiation induced more MB bleaching than spherical Gd-NCPs, which was probably due to the larger water-accessible surface (Figure S6, Supporting Information). Finally, free physcion and Phy@PLGdH were co-incubated with CT26 tumor cells for 24 h to detect intracellular 6PGD enzyme activity. As shown in Figure 3f, Phy@PLGdH and physcion exhibited similar 6PGD inhibition ability, suggesting that physcion incorporated within PLGdH maintained its enzyme inhibitory activity. Overall, these results presumably suggested that Phy@PLGdH nanosheets would be a well-designed radiosensitizer via combination of high-Z strategy and regulation of pentose phosphate pathway.

## 2.2. Cellular Radiosensitization by Phy@PLGdH Nanosheets

Radiosensitization effects of Phy@PLGdH nanosheets were evaluated upon CT26 tumor cells in vitro. As shown in Figure 4a, after 4 h of coculture, Phy@PLGdH nanosheets were effectively endocytosed (green fluorescence of Phy) by CT26 cells, which were mainly colocalized with lysosomes (LysoTracker Red). NADPH was an important reducing equivalent, profoundly involving in GSH synthesis, regeneration, and subsequent radioresistance (Figure 4b). As PPP is the largest contributor of cytosolic NADPH,<sup>[10a]</sup> the levels of NADPH and GSH were found to decrease significantly after Phy@PLGdH nanosheet treatment, which indicated that the redox homeostasis of CT26 tumor cells was destructed (Figure 4c,d). To further investigate whether NADPH and GSH elimination would lead to enhanced oxidative stress upon RT, 2',7'-dichlorodihydrofluorescein diacetate (H<sub>2</sub>DCFDA) was used as a ROS indicator. Owing to efficient X-ray deposition, brighter green fluorescence of ROS could be observed in PLGdH+RT-treated cells, when compared with RT alone (Figure 4e,f). Additionally, the ROS fluorescence intensity was further augmented by Phy@PLGdH+RT treatment, demonstrating that the destruction of redox homeostasis caused by PPP intervention amplified the oxidative stress of high-Z radiosensitization. Notably, PLGdH-sensitized RT produced more ROS than spherical Gd-NCPs at equivalent Gd dose (Figure S7, Supporting Information), confirming their better performance of in amplifying RT-mediated oxidative stress again.

Since the regulation of the PPP would significantly affect ribose synthesis (raw materials for DNA repair),<sup>[15d]</sup> we further evaluated the repair kinetics of DNA double-strand breaks after Phy@PLGdH-sensitized RT. As shown in Figure 4g,h, Phy@PLGdH+RT induced more  $\gamma$ H<sub>2</sub>AX foci (a marker of DNA double-strand breaks) than PLGdH+RT or RT alone via

synergetic high-Z radiosensitization and destruction of redox homeostasis. Then,  $\gamma$ H<sub>2</sub>AX foci in PLGdH+RT-treated cells decreased rapidly and almost completely disappeared within 12 h, which was similar with it at RT alone. However, due to the inhibition of ribose supply, the change of  $\gamma$ H<sub>2</sub>AX foci in Phy@PLGdH+RT-treated cells was slower. Thus, these results confirmed that Phy@PLGdH could enable tumor cells to suffer from more severe oxidative stress and sustained DNA damage after RT.

Subsequently, we assessed the therapeutic cytotoxicity of Phy@PLGdH-nanosheet-sensitized RT upon CT26 tumor cells. As shown in Figure S8 (Supporting Information), no obvious cytotoxicity could be detected in tumor cells treated by PLGdH nanosheets, potentially indicating their great biocompatibility. After incorporation with 6PGD inhibitor physcion, Phy@PLGdH nanosheets inhibited the growth of tumor cells weakly (Figure S9, Supporting Information). Then, PLGdH nanosheets significantly enhanced the outcome of RT in a dose-dependent manner, which was primarily attributed to more ROS production via high-Z radiosensitization. In addition, the stronger anti-tumor effect of PLGdH+RT than Gd-NCPs+RT demonstrated the advantage of nanosheets in depositing X-rays (Figure 4i). By destructing the redox and nucleotide homeostasis, Phy@PLGdH obviously improved their radiosensitizing activity, and exhibited much stronger cytotoxicity against CT26 tumor cells. Finally, the cell cloning assay was performed to evaluate the impact of Phy@PLGdH-sensitized RT on tumor cell proliferation for a long period of time. Compared with RT alone, Phy@PLGdH-sensitized RT effectively weakened the clone forming of tumor cells with almost no spot being observed (Figure 4j,k). Therefore, these results showed that the intervention of PPP could markedly potentiate high-Z radiosensitization for effective proliferation inhibition.

## 2.3. Radiosensitization of Phy@PLGdH in Tumor 3D Spheroids

Since nanosheets were reported with better tumor tissue penetrability than nanoparticles in some studies,<sup>[18]</sup> we evaluated the transport dynamics of PLGdH nanosheets through CT26 multicellular 3D spheroids. Indocyanine green (ICG) was incorporated into spherical Gd-NCPs and sheet-like PLGdH as the fluorescent probe. After 8 h of incubation, CT26 tumor 3D spheroids treated with ICG@Gd-NCPs exhibited red fluorescence only in the margin areas. Conversely, ICG@PLGdH nanosheets showed stronger red fluorescence and penetrated throughout the whole spheroids (Figure 5a). Dynamic fluorescence intensity at 40  $\mu$ m section further confirmed that sheet-like ICG@PLGdH exhibited deeper penetration than spherical Gd-NCPs (Figure 5b).

We further detected the therapeutic cytotoxicity of Phy@PLGdH-sensitized RT within CT26 tumor 3D spheroids. Due to the better penetrability and X-ray deposition, PLGdH-sensitized RT obviously caused more dead tumor cells (propidium iodide (PI<sup>+</sup>) tumor cells) within 3D spheroids than RT alone. After cooperation with PPP intervention, the radiosensitization effect had been more significantly improved (Figure 5c,d). Furthermore, the recorded spheroid growth curves also indicated that Phy@PLGdH nanosheets remarkably enhanced

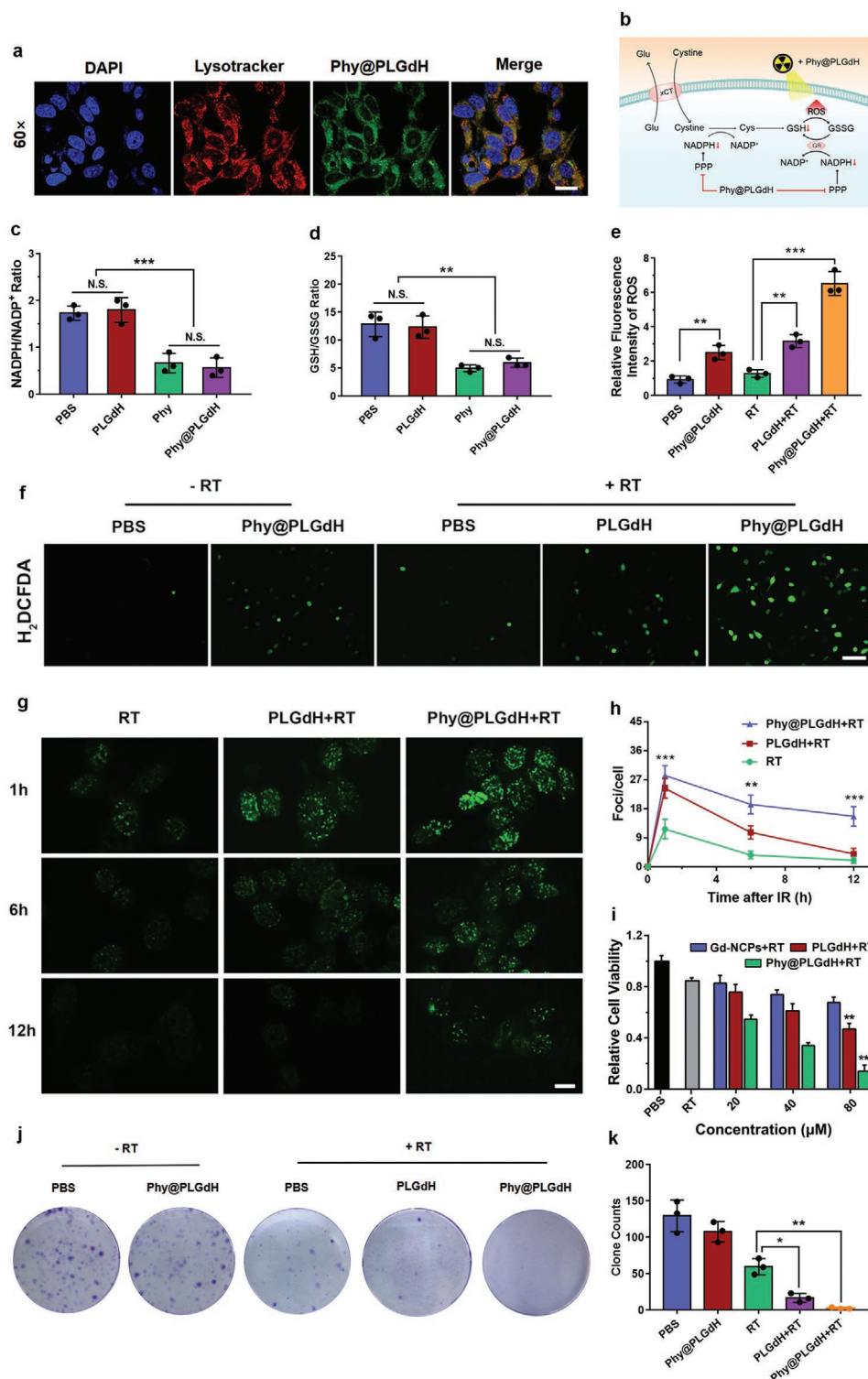


**Figure 4.** Cellular radiosensitization by Phy@PLGdH nanosheets. a) Confocal laser scanning microscopy (CLSM) images of CT26 cells treated with DAPI, LysoTracker (red fluorescence), and Phy@PLGdH (green fluorescence of Phy), respectively. The yellow regions indicate colocalization of Phy@PLGdH with lysosomes. Scale bar = 15 μm. b) Phy@PLGdH nanosheets inhibited GSH synthesis and regeneration. c,d) Phy@PLGdH nanosheets decreased cellular NADPH/NADP<sup>+</sup> and GSH/GSSG ratios within CT26 cells. Data are shown as mean ± SD (*n* = 3, one-way ANOVA). e,f) Fluorescence images and quantification of intracellular ROS level in CT26 cells with RT (0 or 6 Gy). Data are shown as mean ± SD (*n* = 3, one-way ANOVA). Scale bar = 100 μm. g,h) Fluorescence images and quantification of γ-H<sub>2</sub>AX foci in CT26 cells at 1, 6, and 12 h after RT (6 Gy). Data are shown as mean ± SD (*n* = 3, one-way ANOVA). Scale bar = 30 μm. i) Cytotoxicity of Gd-NCPs, PLGdH, Phy@PLGdH with RT (6 Gy) upon CT26 cells. ([Gd] = 20 × 10<sup>-6</sup>, 40 × 10<sup>-6</sup>, 80 × 10<sup>-6</sup> M). Data are shown as mean ± SD (*n* = 3, one-way ANOVA). j,k) Representative images and quantification of CT26 cell clones after different treatments. Data are shown as mean ± SD (*n* = 3, one-way ANOVA). N.S. represents nonsignificance, and \**p* < 0.05; \*\**p* < 0.01; \*\*\**p* < 0.001.

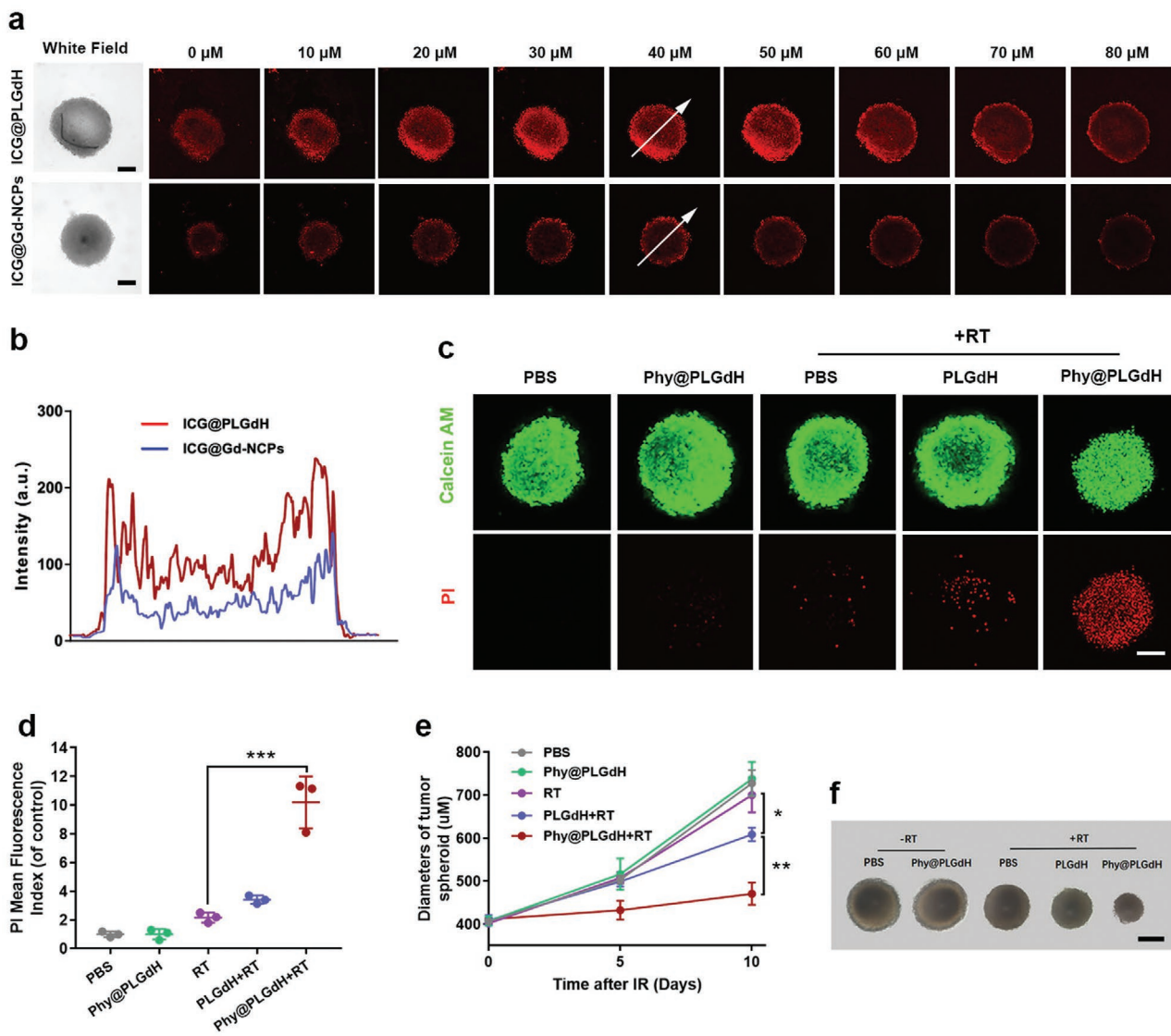


**Figure 5.** Penetration and therapeutic efficacy of Phy@PLGdH-sensitized RT in tumor 3D spheroids. a) Penetration of ICG@Gd-NCPs nanoparticles and ICG@PLGdH nanosheets within CT26 tumor 3D spheroids. Scale bar = 200  $\mu\text{m}$ . b) Dynamic ICG fluorescence intensity profile along with the white arrows. c) Calcein-AM/PI staining images of CT26 tumor spheroids after different treatments. Scale bar = 200  $\mu\text{m}$ . Green: living cells labeled by Calcein-AM, red: dead cells labeled by PI. d) Relative PI mean fluorescence index of CT26 tumor spheroids based on (c). Data are shown as mean  $\pm$  SD ( $n = 3$ , one-way ANOVA). e) Growth curves of CT26 tumor spheroids treated by PBS, PLGdH, and Phy@PLGdH with RT (0 or 6Gy). Data are shown as mean  $\pm$  SD ( $n = 3$ , one-way ANOVA). f) Representative images of CT26 tumor 3D spheroids at day 10 after various treatments. Scale bar = 400  $\mu\text{m}$ . N.S. represents nonsignificance, and \* $p < 0.05$ ; \*\* $p < 0.01$ , \*\*\* $p < 0.001$ .

radiosensitized effects of tumor spheroids, and resulted in the highest growth inhibition at 10th day (Figure 5e,f).

#### 2.4. ICD Induction via Phy@PLGdH-Sensitized Radiation Therapy

Insufficient immunogenic cell death induced by RT alone impedes the activation of antitumor immunity. Encouraged by the outstanding performance of Phy@PLGdH-sensitized RT in oxidative stress and DNA damage induction, we then examined whether Phy@PLGdH nanosheets could enhance RT-induced ICD. Compared with other treatments, Phy@PLGdH-sensitized

radiation therapy significantly induced the exposure of CRT on the surface of stressed tumor cells, acting as an “eat me” signal to potentially improve the phagocytosis of dying tumor cells by dendritic cells (DCs) (Figure 6a,b). Meanwhile, western blotting analysis (Figure 6c) revealed that tumor cells treated with Phy@PLGdH+RT exhibited the highest expression of C/EBP homologous protein (CHOP), a representative marker of endoplasmic reticulum (ER) stress. These results suggested that overproduced ROS mediated by Phy@PLGdH+RT effectively induced CRT exposure by causing ER stress. In addition, the release of other ICD markers, including HMGB1 and ATP in Phy@PLGdH+RT group were also apparently increased, which were beneficial for DC maturation (Figure 6d,e).

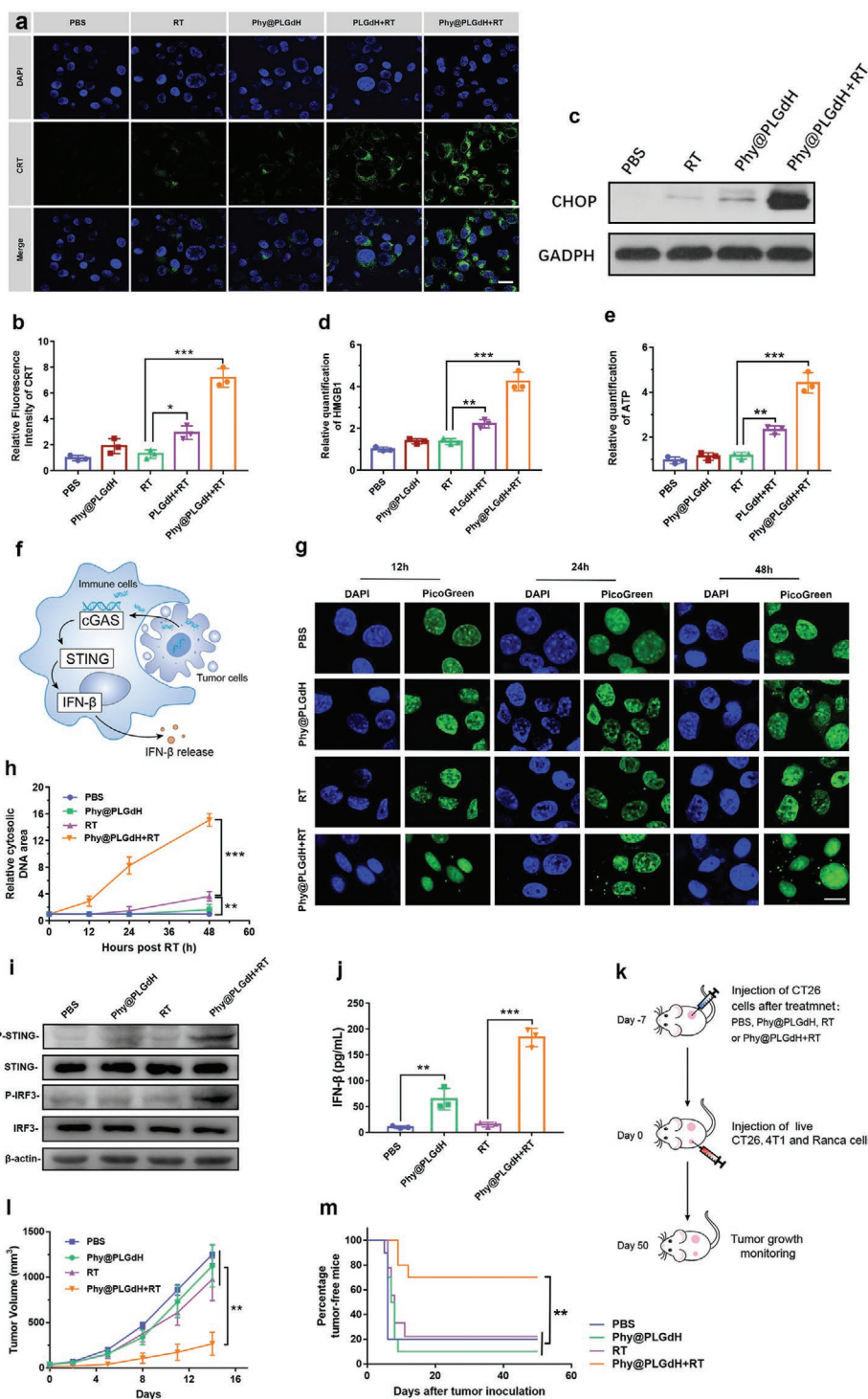


**Figure 6.** Immunogenic cell death induction. a) Immunofluorescence of CT26 tumor cells stained with anti-CRT antibody. Scale bar = 50  $\mu\text{m}$ . b) Quantification of relative CRT means fluorescent intensity based on (a). Data are shown as mean  $\pm$  SD ( $n = 3$ , one-way ANOVA). c) Western blot of CHOP. d) Detection of extracellular and cytosolic HMGB1 by ELISA kit. Data are shown as mean  $\pm$  SD ( $n = 3$ , one-way ANOVA). e) Detection of ATP secretion by luciferin-based ATP assay kit. Data are shown as mean  $\pm$  SD ( $n = 3$ , one-way ANOVA). f) Illustration of IFN- $\beta$  secretion. g) Representative images of DAPI-stained (blue) and PicoGreen-stained (green) CT26 tumor cells at various time points after different treatments. Scale bar = 10  $\mu\text{m}$ . h) Quantification of relative DNA damage area to the total nuclei area stained by PicoGreen in (g). Data are shown as mean  $\pm$  SD ( $n = 3$ , one-way ANOVA). i) Western blot of p-STING, STING, p-IRF3, IRF3, and  $\beta$ -actin. j) The IFN- $\beta$  secretion from cocultured Raw264.7 and CT26 cells after different treatments. Data are shown as mean  $\pm$  SD ( $n = 3$ , one-way ANOVA). k) Schematic illustration of prophylactic tumor vaccination model. l, m) The growth curves (l) and Kaplan–Meier tumor-free curves (m) of tumors in the right flank of mice. Data are shown as mean  $\pm$  SD ( $n = 10$ , one-way ANOVA). N.S. represents nonsignificance, and \* $p < 0.05$ ; \*\* $p < 0.01$ ; \*\*\* $p < 0.001$ .

Except for inducing DNA damage, PPP intervention could also delay the repair process of damaged DNA by inhibiting ribose synthesis. These synergistic effects potentially result in more DNA fragments being released into cytoplasm or extracellular spaces, which could potentially activate the cyclic guanosine monophosphate-adenosine monophosphate synthase/interferon gene stimulator (cGAS–STING) pathway of surrounding immune cells to improve type I interferons (IFN-I) secretion (Figure 6f). We then evaluated the accumulation of cytosolic DNA fragments after various treatments via PicoGreen, a dye for quantifying double-stranded DNA (dsDNA). As shown in Figure 6g,h, Phy@PLGdH+RT significantly induced the accumulation of cytosolic DNA fragments, when compared with other three treatments. Then, we also investigated whether the cGAS–STING pathway could be activated after treatment. 24 h after RT, the treated CT26 tumor cells were cocultured with Raw264.7 cells (monocyte/macrophage-like cells) and incubated for another 24 h. As shown in Figure 6i, Phy@PLGdH+RT remarkably upregulated the phosphorylation levels of STING, and interferon regulate factor 3 (IRF-3) of the cocultured cells. Meanwhile, the content of IFN- $\beta$  in supernatant was also obviously elevated (Figure 6j), indicating that the cytosolic DNA fragments induced by Phy@PLGdH+RT sequentially activated cGAS–STING pathway for subsequent IFN-I secretion. Next, we performed ICD tumor vaccination in syngeneic mice, which was deemed to be the gold standard for assessing ICD induction in vivo. In this experiment, CT26 tumor cells treated with phosphate-buffered saline (PBS) and Phy@PLGdH with or without RT were vaccinated subcutaneously in the left flank of immunocompetent BALB/c mice. Ten days later, the mice were rechallenged with live CT26 tumor cells in the right flank (Figure 6k). As shown in Figure 6l,m, mice vaccinated with Phy@PLGdH+RT-treated CT26 cells presented a significant retardation in tumor growth (Figure 6l) and resulted in 70% of tumor-free (Figure 6m). By contrast, neither Phy@PLGdH nor RT alone show obvious differences with PBS treatment. However, the prevaccination of Phy@PLGdH+RT-treated CT26 cells could not remarkably slow down the growth of 4T1 (breast cancer cells) and Ranca (renal carcinoma) tumors, indicating that this vaccine effect induced by Phy@PLGdH+RT-treated CT26 cells was CT26 cell-specific (Figure S10, Supporting Information). Altogether, these results indicated that Phy@PLGdH-sensitized RT rendered tumor cells more immunogenic and resulted in a potent vaccine effect for potentially initiating systemic antitumor immunity in vivo.

## 2.5. In Vivo Behavior of Phy@PLGdH Nanosheets

We next assessed the plasma clearance and tumor accumulation kinetics of Phy@PLGdH nanosheets. After intravenous (i.v.) injection (free [Phy] = 14 mg kg<sup>-1</sup>) or Phy@PLGdH nanosheets ([Gd] = 30 mg kg<sup>-1</sup>, [Phy] = 14 mg kg<sup>-1</sup>), free phycion was quickly eliminated from blood circulation ( $t_{1/2}$  = 2.04 h), and Phy@PLGdH nanosheets significantly improved the circulation time of phycion ( $t_{1/2}$  = 7.39 h) (Figure 7a,b). Then, Gd exhibited similar pharmacokinetic behavior with Phy in Phy@PLGdH nanosheets, potentially indicating their in vivo biostability (Figure 7c). The established Phy@PLGdH nanosheets

obviously accumulated within tumor tissues, and peaked at 6 h postadministration, which should be potentially attributed to their extended half-life (Figure 7d,e). We further assessed the in vivo behaviors of Phy@PLGdH via MRI, where Gd in Phy@PLGdH nanosheets was used as the contrast agent. As shown in Figure 7f,g, the dynamic MR signal in the tumor regions also confirmed the accumulation of Phy@PLGdH nanosheets. Meanwhile, we observed that MR signal of kidneys reached the maximum at 24 h post-injection and then gradually decreased, potentially indicating the renal clearance of Phy@PLGdH nanosheets (Figure 7f,g). If a large amount of free Gd<sup>3+</sup> was excreted from the kidneys, it might cause obvious damage to kidney tissues. When daily i.v. injected with the same dose of GdCl<sub>3</sub> and Phy@PLGdH nanosheets ([Gd] = 30 mg kg<sup>-1</sup>) for 7 days, the kidneys of GdCl<sub>3</sub>-treated mice showed serious damage with the atrophy of glomerulus, the abscission of epithelial cells, and the infiltration of inflammatory cells. By contrast, the kidneys of mice treated with Phy@PLGdH nanosheets stayed healthy without observable lesions (Figures S11 and S12, Supporting Information), preliminarily indicating that these injected nanosheets would not mainly be excreted from kidneys in free state of Gd. To further verify the state of metabolic Gd, mouse urine within 48 h after administration of Phy@PLGdH ([Gd] = 30 mg kg<sup>-1</sup>) was collected for dialysis (24 h, Solarbio, 1.0 kDa). The free state of Gd<sup>3+</sup> would be dialyzed out from the dialysis bag, while the nanosized or coordinated Gd would be retained within the dialysis bag. Then, the urine in dialysis bag and dialysate (outside of dialysis bag) were separately analyzed by inductively coupled plasma optical emission spectroscopy (ICP-OES) for Gd detection. The results indicated that 408.7  $\mu$ g Gd in coordination state was found in the urine sample within dialysis bag. However, only 13.3  $\mu$ g free Gd<sup>3+</sup> was detected from dialysate, which was almost negligible. Therefore, within 48 h after injection, 421.0  $\mu$ g of Gd (70.2% of 600.0  $\mu$ g Gd per mouse injected) was excreted into the urine, and 97.1% of the excreted Gd was in coordination state (Figure 7h). Some studies have reported that nanoparticles larger than 15 nm (hydrodynamic diameter) could not be rapidly and effectively cleared out by the kidneys. Then, we revealed the degradation process of Phy@PLGdH nanosheets in vitro. Specifically, we used 50% FBS as the simulated plasma to continuously dilute Phy@PLGdH and monitored their size change profiles. During the dilution process, we found that the hydrodynamic diameter of Phy@PLGdH was gradually decreased from 164.6 to 13.1 nm (Figure 7i). Therefore, these results indicated that Phy@PLGdH could be disintegrated to much smaller nanosheets or coordination complexes and then gradually filtered out into the urine.

## 2.6. Activation of Antitumor Immune Response

Subsequently, we assessed the radiosensitization effects of Phy@PLGdH nanosheets upon CT26-tumor-bearing mice. The treatment schedule was shown in Figure 8a. As shown in Figure S13 (Supporting Information), PLGdH and Phy@PLGdH themselves did not have obvious therapeutic effects on tumor growth. However, when combined with RT, PLGdH nanosheets suppressed tumor growth more obviously than RT alone, suggesting their radiosensitization effects based on

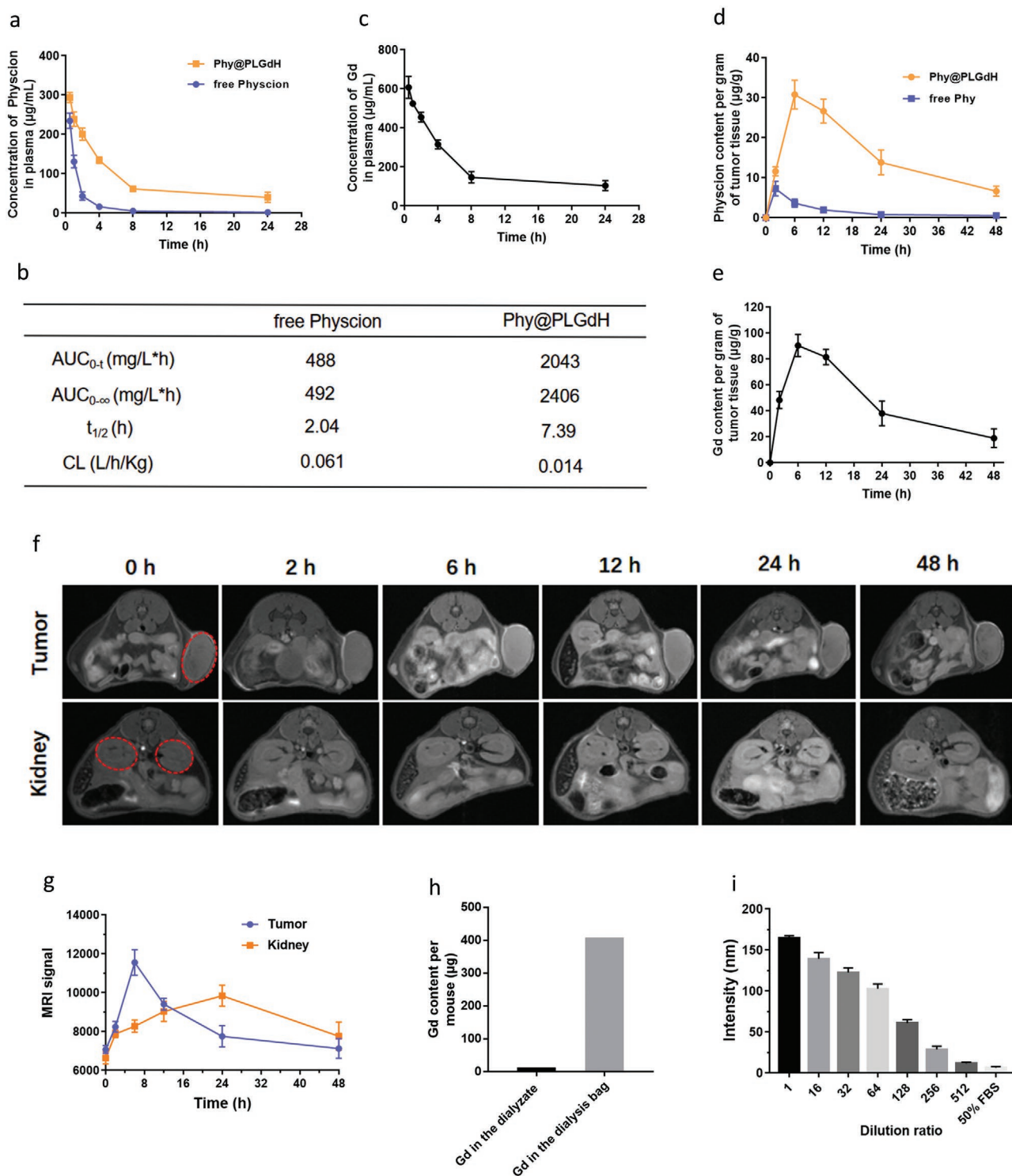


**Figure 7.** a,b) Pharmacokinetics (a) and pharmacokinetic parameters (b) of free physcion and Phy@PLGdH nanosheets after intravenous administration. c) Pharmacokinetic profile of Gd from Phy@PLGdH nanosheets. d,e) The dynamic concentrations of free physcion and Phy@PLGdH accumulated within tumor tissues. Data are shown as mean  $\pm$  SD ( $n = 3$ ). f) Dynamic MR images after intravenous injection of Phy@PLGdH ( $[\text{Gd}] = 30 \text{ mg kg}^{-1}$ ), and the dashed red circles indicated tumors and kidneys, respectively. g) MRI signal of tumors and kidneys based on MR images (f) at different time points. Data are shown as mean  $\pm$  SD ( $n = 3$ ). h) Content of Gd in mouse urine detected by ICP-OES. i) Change of hydrodynamic diameters of Phy@PLGdH nanosheets during the continuous dilution by 50% FBS. Data are shown as mean  $\pm$  SD ( $n = 3$ ).

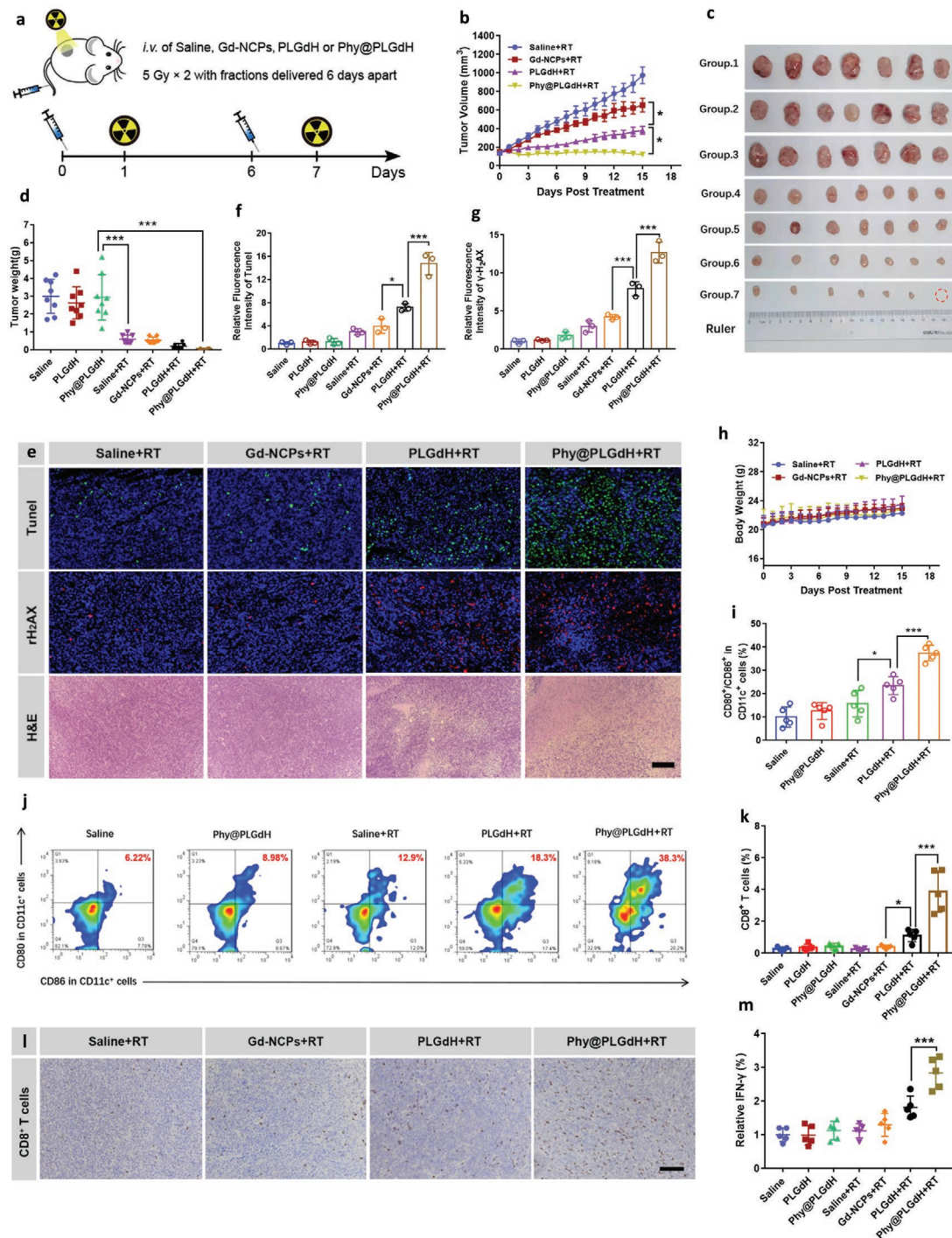


**Figure 8.** Therapeutic efficacy of Phy@PLGdH-sensitized RT upon CT26-bearing mice. a) Schematic illustration of tumor therapeutic profiles. CT26-tumor-bearing mice treated with Saline, PLGdH, Phy@PLGdH, Saline+RT, Gd-NCPs+RT, PLGdH+RT, Phy@PLGdH+RT (Groups 1–7, [Gd] = 30 mg kg<sup>-1</sup>, [physcion] = 14 mg kg<sup>-1</sup>). RT 5 Gy × 2 with fractions delivered 6 days apart. b) Tumor growth curves of mice in different groups. Data are shown as mean ± standard error of the mean (S.E.M.) (n = 7, one-way ANOVA). c) Images of tumor tissues collected on day 15 in different groups. d) Tumor weights of mice in different groups. Data are shown as mean ± SD (n = 7, one-way ANOVA). e) Immunofluorescence images of tumor slices stained with anti-γH<sub>2</sub>AX antibody, TUNEL assay kit, and H&E. Scale bar = 50 μm. f, g) Quantification of TUNEL, γH<sub>2</sub>AX mean fluorescence intensity based on (e). Data are shown as mean ± SD (n = 7, one-way ANOVA). h) Body weights of mice during various treatments. Data are shown as mean ± SD, n = 7. i) The proportion of mature DCs (CD80<sup>+</sup>/CD86<sup>+</sup> gated in CD11c<sup>+</sup>) in tumor-draining lymph nodes detected by flow cytometry. Data are shown as mean ± SD (n = 5, one-way ANOVA). j) Representative flow cytometry dot plot of mature DCs. k) The percentages of tumor-infiltrated CD8<sup>+</sup> T cells detected by flow cytometry. Data are shown as mean ± SD (n = 5, one-way ANOVA). l) Representative images of the immune histochemical staining of infiltrated CD8<sup>+</sup> T cells. Scale bar = 100 μm. m) Intratumoral IFN-γ levels in various groups. Data are shown as mean ± SD (n = 5, one-way ANOVA). N.S. represents nonsignificance, and \*p < 0.05; \*\*\*p < 0.001.

their excellent X-ray deposition. We then compared the radiosensitization effects between sheet-like PLGdH and spherical Gd-NCPs, respectively. Probably owing to the superior X-ray deposition and penetrability, PLGdH+RT slowed the tumor growth more significantly than Gd-NCPs+RT (Figure 8b,c). After coupling with PPP intervention, Phy@PLGdH nanosheets further improved the radiosensitization effects and exhibited the most significant therapeutic effects (Figure 8b–d).

The tumor tissues of mice on day 15 were harvested for TUNEL,  $\gamma$ H<sub>2</sub>AX, hematoxylin and eosin (H&E) staining (Figure 8e and Figure S14 (Supporting Information)). The staining images and quantification of terminal deoxynucleotidyl transferase dUTP nick-end labeling (TUNEL) (Figure 8f) and  $\gamma$ H<sub>2</sub>AX (Figure 8g) showed that Phy@PLGdH significantly promoted RT-mediated apoptosis and DNA double-strand breaks. H&E staining images also indicated that after the treatment of Phy@PLGdH+RT, tumor tissues exhibited the largest area of necrosis and cell nucleus dispersion in all groups. In addition, no significant difference in body weights (Figure 8h), histological analysis of major organs (Figure S15, Supporting Information), and serum biochemistry (Figure S16, Supporting Information) in all groups preliminarily indicated the excellent biosafety of Phy@PLGdH nanosheets.

We then evaluated the activation of antitumor immune response induced by Phy@PLGdH-sensitized radiation therapy. Due to ICD induction, we detected the population of mature DCs within tumor draining lymph nodes (TDLNs) by flow cytometry. Phy@PLGdH+RT induced 38.3% DC maturation in TDLNs (CD80<sup>+</sup>/CD86<sup>+</sup> gated in CD11c<sup>+</sup>), which was significantly higher than those in RT (12.9%) or PLGdH+RT (18.3%) groups on day 5 after irradiation (Figure 8i,j). Furthermore, we assessed the proportion of infiltrated CD8<sup>+</sup> T cells within tumors tissues on day 15 (Figure 8b). Compared with other treatments, Phy@PLGdH+RT induced the most CD8<sup>+</sup> T cells' infiltration (Figure 8k,l and Figures S17 and S18 (Supporting Information)) and IFN- $\gamma$  secretion (Figure 8m). These results implied that Phy@PLGdH-sensitized RT would play a crucial role in initiating adaptive immune responses to potentially prevent systemic metastatic tumors.

## 2.7. Therapeutics of Systemic Tumor Metastasis

Encouraged by attractive performance of Phy@PLGdH+RT in priming antitumor immunity, Phy@PLGdH-sensitized RT was further challenged to treat metastatic triple-negative breast cancer (4T1) tumor model with poor immunogenicity (Figure 9a). For primary 4T1 tumors, as shown in Figure 9b and Figure S19 (Supporting Information), Phy@PLGdH+RT significantly slowed the progression of 4T1 tumors than RT alone (tumor growth inhibition, TGI 79.1% vs 51.9%). To observe the spontaneous metastasis of these mice over a long period, we excised their primary tumors on day 21 and then monitored the body weight of each mouse every day. Probably, for the increasing metastatic burden within their normal organs, the body weights of mice in both Saline and Saline+RT groups decreased gradually from day 25 (Figure 9c), and died within 65 days. However, 5/8 (62.5%) mice in Phy@PLGdH+RT group showed stable or increasing body weights, and survived

(Figure 9d–h). Meanwhile, as shown in Figure 9j,k, mice still displayed numerous metastatic foci within their lungs even after RT, suggesting the poor vaccine effect of RT alone. However, in Phy@PLGdH+RT groups, there were only sporadic lung foci observed within mice lungs, which revealed that the synergetic strategy effectively initiated the systemic antitumor immunity for tumor metastasis inhibition.

When CD8<sup>+</sup> T cells were immunodepleted in 4T1-bearing mice by anti-CD8a antibody ( $\alpha$ CD8a), we found that the therapeutic effects of Phy@PLGdH+RT in primary tumors (TGI 29.2%; Figure 9b and Figure S19 (Supporting Information)) and metastatic tumors (Figure 9j,k) were largely erased. Meanwhile, the life spans of the treated mice were also shortened (Figure 9i). These data indicated that CD8<sup>+</sup> T cells were major players in Phy@PLGdH+RT-mediated tumor inhibition. These performances prompted us to assess the synergistic effect of Phy@PLGdH+RT and PD-L1 blockade therapy. Excitedly, a great synergy between Phy@PLGdH+RT and  $\alpha$ PD-L1 could be observed, accounting for 96.8% inhibition rate upon primary tumors (Figure 9b and Figure S19 (Supporting Information)). Furthermore, the antimetastasis effect of Phy@PLGdH+RT was also potentiated by  $\alpha$ PD-L1, conferring the fewest lung foci (Figure 9j,k) and the highest survival rate (Figure 9i), respectively. Altogether, Phy@PLGdH-sensitized RT could effectively prime the CD8<sup>+</sup>-T-cell-dependent antitumor immune response, and then greatly potentiate PD-L1 blockade therapy against primary and metastatic 4T1 tumors.

## 3. Discussion and Conclusion

Many studies have indicated that effective T-cell priming underlies the success of current tumor immunotherapies (e.g., CBI).<sup>[19]</sup> However, the lack of immunogenicity and adjuvants within TME always lead to poor antigen presentation and DC maturation. Although, in situ vaccination could theoretically provide heterogeneous tumor antigens to prime extensive immune response, the effect is still hindered by immunosuppressive TME.<sup>[20]</sup> Except for releasing numerous tumor antigens, Phy@PLGdH-induced ICD could also successively expose or secrete some inflammatory factors (e.g., CRT, HMGB1, and ATP). Of note, due to the PPP intervention, damaged DNA induced by Phy@PLGdH-sensitized RT strongly elicited the type I interferon response of immune cells within TME for IFN- $\beta$  secretion. IFN- $\beta$  is a key immune-activating reagent bridging innate and adaptive immune responses and favors the antigen cross-presentation in DCs.<sup>[21]</sup> All these events could synergistically result in effective in situ vaccination and improve the immunomodulatory activity of radiation therapy, then increase the response of CBI.

Recently, some nanomaterials (Hensify, AGuIX, and RiMO-301) based on high-Z elements had been explored in clinical trials to boost RT-mediated ICD, but their effectiveness still needed to be improved. Lin and co-workers integrated Hf into nanoscale metal–organic frameworks (Hf<sub>6</sub>-DBA) with ordered and porous structures to enhance the dispersity of Hf clusters for superior X-ray deposition.<sup>[22]</sup> Herein, we optimized high-Z radiosensitization through morphological changes and targeting radioresistant metabolic pathway. For the first time, we

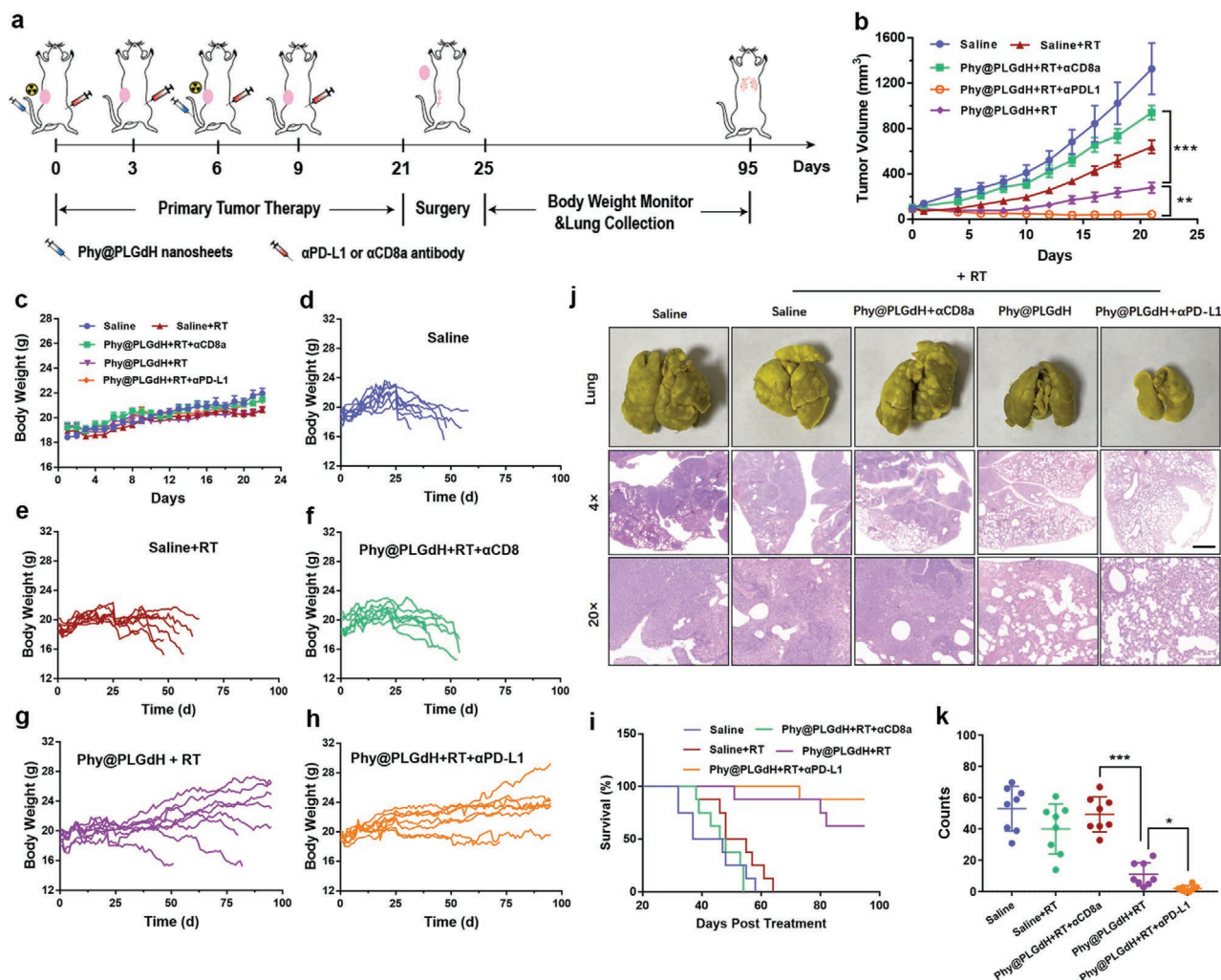


**Figure 9.** Inhibition of metastatic tumors on 4T1 breast tumor model. a) Schematic illustration of tumor therapeutic profile. b) Primary tumor growth curves of 4T1 tumor after treatment of Saline, Saline+RT, Phy@PLGdH+RT+ $\alpha$ CD8, Phy@PLGdH+RT, Phy@PLGdH+RT+ $\alpha$ PD-L1. Treatments were performed on days 0 and 6. RT 6 Gy  $\times$  2 with fractions delivered 6 days apart. Antibodies were treated via intraperitoneal injection 6 h after RT. Data are shown as mean  $\pm$  S.E.M. ( $n = 8$ , one-way ANOVA). c) Dynamic body weights of 4T1-tumor-bearing mice before the surgery. Data are shown as mean  $\pm$  SD,  $n = 8$ . d–h) Body weights of individual 4T1-tumor-bearing mice during the treatments. i) Survival curves for mice bearing 4T1 breast tumors. j) Images of lungs fixed by Bouin's solution and their H&E sections. Scale bar = 1 mm (black). Scale bar = 200  $\mu$ m (white). k) Quantification of metastatic lesions within lungs of mice in different groups. Data are shown as mean  $\pm$  SD ( $n = 8$ , one-way ANOVA). N.S. represents nonsignificance, and  $*p < 0.05$ ,  $**p < 0.01$ ,  $***p < 0.001$ .

introduced layered rare earth hydroxides (LRHs) to radiation oncology and presented their great advantages of radiosensitization. LRH is a new family of layered inorganic compounds with rare earth properties.<sup>[23]</sup> Different from layered double hydroxides, LRHs can be prepared by single metal,<sup>[24]</sup> which maximally reduces the introduction of nontherapeutic metals and makes them more suitable for medical application *in vivo*. Moreover, LRHs can be exfoliated into nanosheets to expose more metal ions at the water-accessible surface, which is quite meaningful to X-ray deposition. Previous studies have demonstrated that LGdH nanosheets owned better MRI imaging property because they exposed more MR-active Gd ions.<sup>[16]</sup> We now report that PLGdH nanosheets outperform spherical Gd-based nanoparticles in X-ray deposition for more effective ROS generation. Meanwhile, the sheet-like structure also endowed PLGdH stronger penetrability to produce ROS in the depth

of tumor tissues, which could potentially overcome hypoxia-mediated radioresistance.<sup>[25]</sup> Thus, we opened a new window for clinic to improve the therapeutic effects of high-Z-sensitized RT.

Furthermore, we tried to seek other resistant mechanisms weakening high-Z-sensitized RT. Metabolic reprogramming is an emerging hallmark of tumors, which allows tumor cells to meet demands for homeostasis, proliferation, and therapeutic resistance.<sup>[26]</sup> Among these metabolic alterations, pentose phosphate pathway deserves special attention. The data from bioinformatic analysis (Figure S20, Supporting Information) suggested that most genes involved in the PPP were upexpressed in colorectal cancer tissues ( $n = 487$ ), compared with adjacent normal tissues ( $n = 35$ ). And overall survival of patients with some other tumors was also negatively associated with G6PD and 6PGD expression. Meanwhile, increasing evidence

available showed that PPP flux would be elevated by tumor cells to provoke resistance to various tumor therapies.<sup>[27]</sup> Notably, the resistance to RT, a treatment that induces oxidative and DNA damage on cells, is tightly correlated with PPP. PPP served as the first line of defense against oxidative stress.<sup>[14b,28]</sup> For rapid response to RT-induced oxidative stress, a large amount of cytoplasmic NADPH would be consumed by glutathione reductase and thioredoxin reductase to regenerate GSH and Trx for ROS detoxication. In addition to being a product of the PPP, NADPH was also a potent inhibitor of G6PD. The consumption of NADPH would rapidly enhance the G6PD activity and elevate PPP flux to produce more NADPH to support the stabilization of NADPH pool,<sup>[29]</sup> then prevent tumor cells from oxidative damage. Furthermore, the elevated PPP flux would also bring more ribose, which could engage in DNA repair upon RT as building blocks.<sup>[15c]</sup> Therefore, PPP is believed to orchestrate the radiotherapeutic outcomes in clinic deeply, including high-Z-sensitized RT. Correspondingly, our work clearly confirmed that PPP blocking significantly potentiated high-Z-sensitized radiation, especially its immunoregulatory effect, which potentially proposed a favorable combination strategy for high-Z-sensitized RT in clinic.

In addition, all the components from Phy@PLGdH nanosheets were biocompatible. Gd ion was widely used as contrast agent and physcion was screened from 2000 FDA-approved compounds.<sup>[30]</sup> In clinic, kidney injury caused by released Gd ions was one of the major concerns for Gd-based drugs.<sup>[31]</sup> With the modification of OA/PEG, the free Gd<sup>3+</sup> released from PLGdH nanosheets under acidic conditions was significantly decreased, which potentially guaranteed their biological safety in vivo. Besides, we displayed the great potential of PLGdH as a multifunctional drug delivering platform by successfully intercalating other anionic molecules (e.g., fluorescein isothiocyanate, indole green, alcian blue, hemin) into PLGdH nanosheets. However, cation drugs, like acriflavine, failed to be intercalated (Figure S21, Supporting Information), further indicating the drug loading mechanism of LRHs via anionic exchange.<sup>[32]</sup>

In summary, we developed Phy@PLGdH nanosheets aiming to sensitize RT for inducing efficient in situ tumor vaccination. In which, physcion-mediated PPP intervention significantly augmented the therapeutic effect of high-Z-sensitized RT to synergistically induce potent immunogenic death and successfully primed CD8<sup>+</sup>-T-cell-dependent immune response for potentiating CBI against primary and metastatic tumors. The well-designed Phy@PLGdH nanosheets with biocompatibility and therapeutic outcomes potentially provided a novel paradigm for radiosensitization and antitumor immunotherapy.

## 4. Experimental Section

**Materials:** Gadolinium trichloride hexahydrate (GdCl<sub>3</sub>·6H<sub>2</sub>O) was purchased from Energy Chemical (China). Physcion was supplied by Yuanye (China). Sodium oleate was purchased from Aladdin Industrial Corporation (Shanghai, China). DSPE-PEG2000 was supplied by Ponsure Biological (China). 4',6-diamidino-2-phenylindole (DAPI) and LysoTracker Red were obtained from Sigma-Aldrich (USA). glutathione (GSH) and oxidized glutathione (GSSG) Assay Kit and ATP Assay Kit were purchased from Beyotime Biotech Inc. (China). H<sub>2</sub>DCFDA was

supplied by KeyGEN Biotech (China). Cell Counting Kit-8 (CCK-8) was obtained from Dojindo Laboratories (Japan). IRF-3 antibody (D83B9, CST), p-IRF-3 antibody (D6O1M, CST), STING antibody (DIV5L, CST), p-STING (D8F4W, CST), β-actin antibody (13E5, CST), PicoGreen (Yeasen, China). Mouse IFN-γ-precoated enzyme-linked immunosorbent assay (ELISA) Kit was obtained from DAKWEI (China). Mouse HMGB1 ELISA Kit was obtained from Yifeixue Biotechnology (China). Anti-Calreticulin-ER Marker (Alexa Fluor 488), anti-gamma H2AX (phospho S139) antibody [9F3], TUNEL Assay Kit – BrdU-Red, and Anti-Ki67 antibody were supplied by Abcam (USA). PE anti-mouse CD3 antibody, APC anti-mouse CD8a antibody, PE anti-mouse CD80 antibody, Alexa Fluor 647 anti-mouse CD86 antibody, Alexa Fluor 488 anti-mouse CD11c antibody, and Ultra-LEAF Purified anti-mouse CD8a (clone: 53-6.7) were purchased from BioLegend (USA). In vivo MAb anti-mouse PD-L1(B7-H1) (clone: 10F.9G2) was purchased from BioXcell (USA). The mouse CT26 colorectal cancer cells and 4T1 breast cancer cells were purchased from China Type Culture Collection, supplied by the American Type Culture Collection. BALB/c mice were obtained from the Yangzhou University Medical Centre (China).

**Preparation of LGdH ([Gd<sub>2</sub>(OH)<sub>5</sub>(H<sub>2</sub>O)<sub>4</sub>]Cl):** Preparation of LGdH was typically performed as follows. First, NaOH solution (0.10 M, 20 mL) was added to GdCl<sub>3</sub>·6H<sub>2</sub>O solution (0.05 M, 20 mL) dropwise with vigorous stirring at room temperature. Then, the mixed solutions were heated to 60 °C for 12 h and refluxed for 24 h with stirring. A slurry of the generated LGdH was collected by centrifuging (12 000 rpm, 15 min) and washed with deionized water for 3 times. The powders of LGdH were obtained and dried at 65 °C.

**Preparation of PLGdH and Phy@PLGdH Nanosheets:** LGdH powders (2.00 g) were dispersed in an aqueous solution (100 mL) containing sodium oleate (OA, 4.00 g) and stirred at room temperature for 12 h. The resulting OA-LGdH was isolated by filtration and washed with deionized water for several times. Then, OA-LGdH (30 mg) powders were mixed with DSPE-PEG (90 mg) in a CHCl<sub>3</sub> suspension and the solvent was removed completely by rotary evaporator. Distilled water (50 mL) was added to disperse the reaction mixture under ultrasound to obtain PEGylated LGdH nanosheets. To exchange physcion into the interval of PLGdH nanosheets, physcion was mixed with OA-LGdH and DSPE-PEG in a CHCl<sub>3</sub> suspension containing triethylamine. Then, Phy@PLGdH nanosheets were obtained via the similar method.

**Characterization of PLGdH and Phy@PLGdH Nanosheets:** The morphology and thickness of PLGdH and Phy@PLGdH nanosheets were characterized by the field emission scanning electron microscopy (GeminiSEM 500, Carl Zeiss, Germany) and Bruker Multimode 8 microscope with ScanAsyst in air mode. Particle sizes and zeta potentials of LGdH, PLGdH, and Phy@PLGdH nanosheets were determined by DLS (Malvern Instruments, Malvern, UK). The zeta potential of nanosheets was determined by Smoluchowski model, where the electrophoretic mobility was proportional to both the dielectric constant and the ζ-potential. The stability of LGdH, PLGdH, and Phy@PLGdH nanosheets was also evaluated by DLS under 50% serum for 24 h at 37 °C, respectively. The PXRD was performed on Enraf Noius CAD4/PC X-ray diffractometer. X-ray photoelectron spectroscopy (PHI5000 VersaProbe, ULVAC-PHI, Japan) was applied to perform element analysis of Phy@PLGdH nanosheets. Thermogravimetric analysis was applied to measure the proportion of each component in LGdH, OA-LGdH, PLGdH, and Phy@PLGdH.

**Quantitative Analysis of [Gd] and Physcion in Phy@PLGdH Nanosheets:** The quantity of [Gd] and physcion in Phy@PLGdH nanosheets was determined by colorimetry. Neothorin was used as a colorimetric reagent for free Gd<sup>3+</sup>. A calibration curve was obtained by plotting absorbance of neothorin solution (2 μg mL<sup>-1</sup>, 200 μL) at 652 nm in the presence of various concentrations of [Gd<sup>3+</sup>] (200 μL) and HCl ([HCl] = 20 × 10<sup>-3</sup> M, 400 μL). In addition, the calibration curve was obtained by plotting absorbance of physcion alkaline aqueous solution ([physcion] = 10 × 10<sup>-6</sup>, 20 × 10<sup>-6</sup>, 40 × 10<sup>-6</sup>, 60 × 10<sup>-6</sup>, 80 × 10<sup>-6</sup>, 100 × 10<sup>-6</sup> M) at 507 nm by ultraviolet spectrophotometer. Typically, the molar ratio of Gd to Phy within the obtained Phy@PLGdH nanosheets detected by these quantitative methods was 4:1.

**Release of Gd and Physcion from PLGdH and Phy@PLGdH Nanosheets at Different pH:** To examine the acid resistance, LGdH and PLGdH nanosheets containing 0.6 mg of Gd were dispersed in 1 mL of phthalate buffer at pH 7.4, 6.0, 5.0, and 4.0, and stirred at room temperature. After 0, 1, 2, 4, 6, 12, and 24 h, 100  $\mu$ L of the suspension was collected and centrifuged, and the concentration of Gd ion in the supernatant solution was determined by ICP-OES (Avio 500, USA). To detect the release profiles, Phy@PLGdH nanosheets were packed in dialysis bag (Solarbio, 1.0 kDa), followed by dialysis in PBS at pH 5.0, 6.0, and 7.4, respectively. Dialysates were collected at 2, 4, 8, 12, 24 h for Phy analysis by high-performance liquid chromatography (HPLC, column, Agilent Zorbax SB-C<sub>18</sub>, 4.6 mm  $\times$  150 mm, 5  $\mu$ m, solvent A acetonitrile, solvent B 0.1% phosphoric acid solution, flow rate 1.0 mL min<sup>-1</sup>, wavelength 226 nm).

**Evaluation of RT-Mediated Hydroxyl Radical ( $\cdot$ OH) Generation In Vitro:** To detect the generation of  $\cdot$ OH during irradiation, a classical method based on the decay of MB was used. In brief, H<sub>2</sub>O<sub>2</sub>, Gd-NCPs, or PLGdH nanosheets were added into MB solutions ([Gd] = 20  $\times$  10<sup>-6</sup> M and [MB] = 15  $\mu$ g mL<sup>-1</sup>). After irradiating with various doses (0, 6 Gy, 12 Gy, 24 Gy), the absorption of MB at 664 nm was measured to detect the degradation of methylene blue.

**Cellular Uptake Detection:** CT26 tumor cells were cultured in Dulbecco's modified Eagle medium (DMEM) supplemented with 10% FBS and 1% penicillin-streptomycin solution with 5% CO<sub>2</sub> at 37  $^{\circ}$ C. To inspect the cellular uptake of Phy@LGdH nanosheets, CT26 cells were seeded into confocal dishes with a density of 2  $\times$  10<sup>5</sup> per well. After attachment, cells were incubated with Phy@PLGdH ([Phy] = 40  $\times$  10<sup>-6</sup> M) for 4 h. Then, tumor cells were incubated with LysoTracker (LysoTracker Red, Yeasen, China) for 30 min. Next, the nucleus was stained with DAPI. After this, the images were obtained and analyzed by laser scanning confocal microscopy (FV3000, Olympus, Japan).

**6PGD Assay and Intracellular NADPH/NADP<sup>+</sup> Quantification:** 6PGD activities of CT26 cells treated by PBS, physcion, and Phy@PLGdH nanosheets for 24 h were measured by 6-phosphogluconate dehydrogenase Activity Detection Kit (ZCI Bio, China). To detect the NADPH/NADP<sup>+</sup> ratio in cells, NADP(H) Assay Kit (ZCI BIO, China) was used. CT26 tumor cells were seeded into 6-well plates with a density of 2  $\times$  10<sup>5</sup> per well. After attachment, cells were treated with PBS, PLGdH, physcion, and Phy@PLGdH ([Gd] = 80  $\times$  10<sup>-6</sup> M, [physcion] = 20  $\times$  10<sup>-6</sup> M) for 24 h. Then, the cells were collected to detect NADPH/NADP<sup>+</sup> according to the manufacturer's protocol.

**GSH/GSSG Quantification:** To detect the intracellular GSH/GSSG, the GSSG Assay Kit (Beyotime, China) was used. CT26 tumor cells were seeded into 6-well plates in a density of 2  $\times$  10<sup>5</sup> per well. After attachment, PBS, PLGdH, physcion, and Phy@PLGdH ([Gd] = 80  $\times$  10<sup>-6</sup> M, [physcion] = 20  $\times$  10<sup>-6</sup> M) were added, respectively, and incubated for 24 h. Then, the cells were collected to detect GSH/GSSG according to the manufacturer's protocol.

**Intracellular ROS Generation:** To investigate the generation of ROS after various treatments, CT26 cells were seeded into 96-well plates with a density of 6  $\times$  10<sup>3</sup> per well. After attachment, Gd-NCPs, PLGdH, and Phy@PLGdH ([Gd] = 80  $\times$  10<sup>-6</sup> M, [physcion] = 20  $\times$  10<sup>-6</sup> M) were added and incubated for 12 h. Then, CT26 cells were irradiated with 6 Gy. 2 h after irradiation, all treatments were removed and changed with the fresh DMEM containing H<sub>2</sub>DCFDA (1:1000, KeyGen Biotech, China), and incubated in dark for 1 h. After that, the cells were washed with PBS for 3 times and green fluorescence images were acquired by Nikon Eclipse Ti (Japan).

**DNA Damage Detection:**  $\gamma$ H<sub>2</sub>AX immunofluorescent staining was applied to measure DNA double-strand breaks. CT26 tumor cells were seeded into confocal dish with a density of 2  $\times$  10<sup>5</sup> per well. After attachment, cells were co-incubated with PLGdH ([Gd] = 80  $\times$  10<sup>-6</sup> M) and Phy@PLGdH ([Gd] = 80  $\times$  10<sup>-6</sup> M, [physcion] = 20  $\times$  10<sup>-6</sup> M) for 12 h. After radiation (6 Gy), CT26 cells were stained by  $\gamma$ H<sub>2</sub>AX mouse monoclonal primary antibody (Abcam, USA) and secondary antibody conjugated with Alexa Fluor 488 (Abcam, USA) at 1, 6, 12 h, respectively, and detected by laser scanning confocal microscopy (FV3000, Olympus, Japan). To detect the release of damaged DNA fragments into

cytoplasm, PicoGreen staining was applied. CT26 cells were seeded into confocal dish with a density of 2  $\times$  10<sup>5</sup> per well. After attachment for 12 h, the cells were incubated with different drugs for 12 h. Then, the tumor cells underwent irradiation with a dose of 8 Gy. After the radiation, cells were cultured for another 12, 24, and 48 h, respectively. For the PicoGreen staining, treated CT26 cells were incubated with PicoGreen (dsDNA Quantitation Reagent, Yeasen, 1:200) for 10 min at 37  $^{\circ}$ C. Then, the tumor cells were washed by PBS and stained with DAPI. The fluorescence images were obtained through Olympus FV3000 laser scanning confocal microscope (LSCM) and analyzed with Image J.

**Therapeutic Cytotoxicity:** To investigate the cytotoxicity of PLGdH ([Gd] = 0, 10  $\times$  10<sup>-6</sup>, 20  $\times$  10<sup>-6</sup>, 40  $\times$  10<sup>-6</sup>, 80  $\times$  10<sup>-6</sup>, and 160  $\times$  10<sup>-6</sup> M) and Phy@PLGdH nanosheets ([Gd] = 0, 40  $\times$  10<sup>-6</sup>, 80  $\times$  10<sup>-6</sup>, and 160  $\times$  10<sup>-6</sup> M, [physcion] = 0, 10  $\times$  10<sup>-6</sup>, 20  $\times$  10<sup>-6</sup>, and 40  $\times$  10<sup>-6</sup> M), CT26 cells were seeded into 96-well plates with a density of 6  $\times$  10<sup>3</sup> per well. After attachment, the cells were incubated with various drugs for 24 h. Then, the tumor cell viability was determined by CCK-8 assay (Dojindo, Japan). To investigate the cytotoxicity, CT26 cells were incubated with Gd-NCPs, PLGdH ([Gd] = 20  $\times$  10<sup>-6</sup>, 40  $\times$  10<sup>-6</sup>, and 80  $\times$  10<sup>-6</sup> M) and Phy@PLGdH nanosheets ([Gd] = 20  $\times$  10<sup>-6</sup>, 40  $\times$  10<sup>-6</sup>, and 80  $\times$  10<sup>-6</sup> M, [physcion] = 5  $\times$  10<sup>-6</sup>, 10  $\times$  10<sup>-6</sup>, and 20  $\times$  10<sup>-6</sup> M) for 12 h, irradiated (6 Gy), and then incubated for another 48 h. After that, the cell viability was determined by CCK-8 assay.

**Clone Formation Assay:** CT26 tumor cells were seeded with a density of 1  $\times$  10<sup>5</sup> per well into 12-well plates, and co-incubated with PLGdH ([Gd] = 80  $\times$  10<sup>-6</sup> M) and Phy@PLGdH ([Gd] = 80  $\times$  10<sup>-6</sup> M, [physcion] = 20  $\times$  10<sup>-6</sup> M) for 12 h. 24 h after irradiation (5 Gy), CT26 cells in all groups were collected and reseeded into 6-well plates with a density of 2  $\times$  10<sup>3</sup> per well. Once the cell colonies formed after about 10 days' cultivation, tumor cell clones were detected by crystal violet solution (Beyotime, China).

**Therapeutic Effects of Phy@PLGdH Nanosheets upon 3D Spheroids:** To evaluate the tissue penetration, CT26 cells were seeded into ultralow attachment 96-well plates (Corning, 7007, USA) with a density of 3  $\times$  10<sup>3</sup> per well. ICG was incorporated into PLGdH and Gd-NCPs to obtain ICG@PLGdH and ICG@Gd-NCPs. Then, 3D spheroids were co-incubated with ICG@PLGdH and ICG@Gd-NCPs for 8 h. After that, the red fluorescence of ICG within spheroids was observed by Olympus FV3000 LSCM. To test the cytotoxicity of Phy@PLGdH-sensitized radiation in 3D tumor cell spheroids, CT26 3D spheroids were treated with PLGdH ([Gd] = 80  $\times$  10<sup>-6</sup> M) and Phy@PLGdH ([Gd] = 80  $\times$  10<sup>-6</sup> M, [physcion] = 20  $\times$  10<sup>-6</sup> M) for 12 h and then irradiated (0 or 6 Gy). After 24 h, calcein-AM and PI were used to stain live and dead cells, and recorded the size of tumor spheroids (Nikon, Japan). Meanwhile, the sizes of tumor spheroids after various treatments were measured by Nikon Eclipse Ti (Japan) at days 5 and 10, respectively.

**CRT Exposure Analysis:** CT26 cells were seeded into confocal dishes with a density of 2  $\times$  10<sup>5</sup> per well. After attachment, cells were co-incubated with PLGdH ([Gd] = 80  $\times$  10<sup>-6</sup> M) and Phy@PLGdH ([Gd] = 80  $\times$  10<sup>-6</sup> M, [physcion] = 20  $\times$  10<sup>-6</sup> M) for 12 h. After irradiation (8 Gy  $\times$  1), CT26 cells were cultured for another 8 h, and then incubated with Alexa Fluor 488-CRT antibody (diluted 1:500 with 3% bovine serum albumin, Abcam, USA) for 1 h, stained with DAPI to label nucleus. The immunofluorescence images were obtained via Olympus FV3000 LSCM and analyzed with Image J.

**Detection of HMGB1 and ATP Release:** HMGB1 located in the cytoplasm following the indicated treatments was measured by ELISA kit (Yifeixue Bio, China), according to the manufacturer's protocol. ATP concentrations in the supernatant of tumor cells upon the indicated treatments were measured by ATP Assay Kit (Beyotime, China), according to the manufacturer's protocol. Luminescence and absorbance were measured by microplate reader (VICTOR Nivo).

**Characterization of cGAS-STING Activation and IFN- $\beta$  Secretion:** CT26 cells were seeded into 6-well dishes, with a density of 2  $\times$  10<sup>5</sup> per well. After incubation for 12 h, Phy@PLGdH ([Gd] = 80  $\times$  10<sup>-6</sup> M, [physcion] = 20  $\times$  10<sup>-6</sup> M) was added and incubated for another 12 h. Then, CT26 cells were irradiated with 8 Gy or unirradiated. After radiation, 5  $\times$  10<sup>5</sup> per well Raw264.7 cells were added to co-incubate

for another 24 h. To assay the activation of cGAS–STING pathway, the total proteins of the mixed cells were isolated using the mixture of non-denatured Tissue/Cell Lysate Kit (Solarbio) with broad spectrum protease inhibitor cocktail (ethylenediaminetetraacetic acid (EDTA) free, BOSTER) and broad-spectrum phosphatase inhibitor cocktail (EDTA free, BOSTER). Then, 40 µg protein was used for western blotting analysis (p-STING, STING, p-IRF3, IRF3, β-actin, CST). To detect the release of IFN-β, CT26 cells were seeded into 6-well plates, with a density of  $2 \times 10^5$  per well. After attachment, CT26 cells were incubated with PLGdH ([Gd] =  $80 \times 10^{-6}$  M) and Phy@PLGdH ([Gd] =  $80 \times 10^{-6}$  M, [physcion] =  $20 \times 10^{-6}$  M) over night. Then, tumor cells were irradiated (8 Gy). After 24 h,  $2 \times 10^5$  Raw264.7 cells were added to each well and co-incubated with treated CT26 cells for another 12 h. Finally, IFN-β in supernatants was detected by ELISA kit (Biolegend, USA).

**Radiosensitization of Phy@PLGdH Nanosheets:** All the animals were obtained from Yangzhou University Medical Center (Yangzhou, China). All animal experiments were performed in accordance with the Guidelines for Care and Use of Laboratory Animals of Nanjing University and the experiments were approved by the Animal Ethics Committee of Nanjing University (IACUC-2003068). During the irradiation experiments, a lead plate was set between the mice and radiator, and the hole of the lead plate ensured that only tumor tissues could be irradiated to avoid unnecessary irradiation to other normal organs or tissues.

Male BALB/c mice were subcutaneously injected with  $5 \times 10^5$  CT26 tumor cells in right flank. When the tumor volume reached 100 mm<sup>3</sup>, mice were divided into seven groups including Saline, PLGdH, Phy@PLGdH, Saline+RT, Gd-NCPs+RT, PLGdH+RT, Phy@PLGdH+RT ([Gd] = 30 mg kg<sup>-1</sup>, [physcion] = 14 mg kg<sup>-1</sup>). The maximal physcion loading efficiency in PLGdH nanosheets could be achieved when the molar ratio of Phy to Gd increased to 1:4. Then, the concentration of physcion (molar ratio of Phy to Gd of 1:4, [Gd] 30 mg kg<sup>-1</sup>, and [Phy] 14 mg kg<sup>-1</sup>) within Phy@PLGdH nanosheets was chosen for synergetic tumor therapy. X-ray irradiation (5 Gy × 2) was performed 6 h post-intravenous-injection. Radiation was performed with fractions delivered 6 days apart. Tumor size and body weights of each group were recorded every day. Tumor volume was calculated according to the formula: width<sup>2</sup> × length/2. After 15 days of treatments, mice were sacrificed, H&E, TUNEL, and γH2AX immunofluorescent staining were performed.

**Pharmacokinetic Study of Phy@PLGdH Nanosheets:** To evaluate the plasma clearance of free physcion and Phy@PLGdH after i.v. injection, BALB/c mice were treated with Phy@PLGdH ([Gd] = 30 mg kg<sup>-1</sup> and [Phy] = 14 mg kg<sup>-1</sup>) or physcion ([Phy] = 14 mg kg<sup>-1</sup>, dissolved by 10% dimethyl sulfoxide and 1% tween-80). Then, the blood was collected at 0.5, 1, 2, 4, 8, and 24 h for physcion and Gd detection ( $n = 3$ ). After centrifugation (12 000 rpm, 10 min), the supernatant of the blood was carefully collected and added by extracting solution (HCl ([HCl] =  $10 \times 10^{-3}$  M, 200 µL) and methanol (1.0 mL)) to extract physcion for HPLC analysis. For Gd detection, collected plasma was digested with 5% v/v nitric acid (1.2 mL), followed by centrifugation (12 000 rpm, 10 min) and the supernatant was collected for ICP-OES analysis (Avio 500, USA).

To evaluate the absolute quantification of Phy@PLGdH in tumor tissues, CT26-tumor-bearing mice ( $\approx 200$  mm<sup>3</sup>) were intravenous injected with Phy@PLGdH ([Gd] = 30 mg kg<sup>-1</sup> and [Phy] = 14 mg kg<sup>-1</sup>) or free physcion ([Phy] = 14 mg kg<sup>-1</sup>), respectively. Tumor tissues were, respectively, collected at 0, 2, 6, 12, 24, and 48 h after i.v. injection ( $n = 3$ ). Then, the tumor tissues were crushed, homogenized, and filled to 2 mL. Then, the solution was divided into two equal parts. One (1.0 mL) was added with HCl and methanol mixed solution (1.0 mL) and centrifuged (12 000 rpm, 10 min) to extract physcion for HPLC analysis. The other part was burned and digested, then rediluted to 2.0 mL for Gd detection via ICP-OES.

**The Biodegradation of Phy@PLGdH Nanosheets:** Phy@PLGdH ([Gd] =  $4 \times 10^{-3}$  M and [Phy] =  $1 \times 10^{-3}$  M) was diluted by 50% FBS, and the dilution ratios were 1, 16, 32, 64, 128, 256, and 512, respectively. Then, the hydrodynamic diameters of Phy@PLGdH nanosheets with different concentrations were, respectively, determined by DLS (Brookhaven 90 plus Zeta).

The mouse urine was collected within 48 h post-injection of Phy@PLGdH ([Gd] = 30 mg kg<sup>-1</sup> and [Phy] = 14 mg kg<sup>-1</sup>), and packed into dialysis bags (Solarbio, 1.0 kDa) for 24 h of dialysis. After dialysis, solutions both inside and outside of the dialysis bags were collected and digested with 5% v/v nitric acid for Gd detection by ICP-OES.

**Biodistribution and MR Imaging In Vivo:** To evaluate the biodistribution of Phy@PLGdH in vivo, CT26-tumor-bearing mice (200–300 mm<sup>3</sup>) were treated with Phy@PLGdH via intravenous injection. Mice were anesthetized with isoflurane and fixed in the animal groove. T1-weighted images were carried out on MR scanner (Biospec 7T/20 USR, Germany). Parameters used for T1-weighted imaging were as follows: flip angle = 180, repetition time (TR) = 500 ms, echo time (TE) = 15.0 ms, field of view (FOV) =  $3 \times 3$ , matrix =  $256 \times 256$ , superior–inferior (SI) = 1.0 mm 1.0 mm<sup>-1</sup>, averages = 3, slices = 12, number of excitations (NEX) = 1. Multiple locations of phantom images were observed at 0, 2, 6, 12, 24, and 48 h and analyzed with ImageJ Software and RadiAnt DICOM Viewer.

**Vaccination Effects In Vivo:** To detect the vaccination effects,  $1 \times 10^5$  CT26 cells treated with PBS, Phy@PLGdH, RT, and Phy@PLGdH+RT were injected subcutaneously into the lower flank of BALB/c mice. After 10 days,  $1 \times 10^5$  live CT26 cells were injected in the contralateral flank for monitor. To evaluate whether Phy@PLGdH+RT-induced tumor vaccination was specific,  $1 \times 10^5$  4T1 and Ranca cells were injected in the contralateral flank of mice, which were prevaccinated by PBS- or Phy@PLGdH+RT-treated CT26 cells.

**Evaluation of Antitumor Immune Response:** For the analysis of DC maturation, TDLNs were collected 5 days post different treatments, including Saline, Saline+RT, PLGdH+RT, Phy@PLGdH, and Phy@PLGdH+RT ([Gd] = 30 mg kg<sup>-1</sup>, [physcion] = 14 mg kg<sup>-1</sup>, 5 Gy × 1). The collected lymph nodes were ground and filtered through 100 µm cell strainers to prepare single cell suspensions. Then, the obtained cells were stained with Alexa Fluor 488 anti-mouse CD11c, Alexa Fluor 647 anti-mouse CD86, and PE anti-mouse CD80 antibodies (BioLegend, USA) and then detected by flow cytometry (BD Calibur).

To detect CD8<sup>+</sup> T-cell infiltration, tumors were harvested after different treatments at day 15. The fresh tissues were cut into small pieces and digested with enzyme mixture (neutral protease, collagenase, and hyaluronidase) to prepare single cell suspensions. Then, cells were stained with PE anti-mouse CD3 and APC anti-mouse CD8a (BioLegend, USA) for flow cytometry analysis. Tumors were also collected for immunohistochemical staining to further evaluate tumor infiltration. Furthermore, IFN-γ secreted within tumors was detected by ELISA kits (Dakewe Biotech Co., Ltd.).

**Inhibition of Tumor Metastasis:** Female BALB/c mice were subcutaneously injected with  $5 \times 10^5$  4T1 breast cancer cells in right flank. Then, mice were divided into 5 groups, including Saline, Saline+RT, Phy@PLGdH+RT, Phy@PLGdH+RT+αPD-L1, Phy@PLGdH+RT+αCD8a ([Gd] = 30 mg kg<sup>-1</sup>, [physcion] = 14 mg kg<sup>-1</sup>, [αPD-L1] = 10 mg kg<sup>-1</sup>, [αCD8a] = 10 mg kg<sup>-1</sup>). RT was performed 6 h after i.v. injection of Saline or Phy@PLGdH, respectively. RT 6 Gy × 2 with fractions delivered 6 days apart, and αCD8a (Dakewe Biotech, China) and αPD-L1 antibody (BioXcell, USA) were treated via intraperitoneal injection every 3 days. Then, the tumor size and body weights were daily recorded. At day 22, the primary tumors in all groups were removed via surgery. Besides, lungs of mice were collected and fixed with Bouin's solution after sacrifice for detecting the lung metastatic foci.

**Statistical Analysis:** A two-tailed Student's *t*-test was performed for the comparison of two groups. For multiple comparisons, a one-way or two-way analysis of variance (ANOVA) test was performed. Then, *p* value > 0.05 represented nonsignificance (N.S.), and *p* value < 0.05 represented statistically significant.

## Supporting Information

Supporting Information is available from the Wiley Online Library or from the author.

## Acknowledgements

Y.X.W. and J.C. contributed equally to this work. This article was supported by The National Key Research and Development Program of China (Grant No. 2017YFA0205400) and the Natural Science Foundation of China (NSFC) (Grant Nos. 81603043, 81872811, and 31872755). This project was also supported by the Central Fundamental Research Funds for the Central Universities.

## Conflict of Interest

The authors declare no conflict of interest.

## Data Availability Statement

The data that support the findings of this study are available from the corresponding author upon reasonable request.

## Keywords

immunogenic cell death, in situ tumor vaccination, layered gadolinium hydroxide nanosheets, pentose phosphate pathway

Received: November 29, 2021

Revised: January 18, 2022

Published online:

- [1] a) S. K. Wculek, F. J. Cueto, A. M. Mujal, I. Melero, M. F. Krummel, D. Sancho, *Nat. Rev. Immunol.* **2020**, *20*, 7; b) P. M. K. Westcott, N. J. Sacks, J. M. Schenkel, Z. A. Ely, O. Smith, H. Hauck, A. M. Jaeger, D. Zhang, C. M. Backlund, M. C. Beytagh, J. J. Patten, R. Elbashir, G. Eng, D. J. Irvine, O. H. Yilmaz, T. Jacks, *Nat. Cancer* **2021**, *2*, 1071.
- [2] a) H. W. Li, J. Y. Yu, Y. Y. Wu, B. Shao, X. W. Wei, *J. Cell. Physiol.* **2020**, *235*, 5490; b) R. H. Pierce, J. S. Campbell, S. I. Pai, J. D. Brody, H. E. K. Kohrt, *Hum. Vaccines Immunother.* **2015**, *11*, 1901.
- [3] a) L. Hammerich, T. U. Marron, R. Upadhyay, J. Svensson-Arvelund, M. Dhainaut, S. Hussein, Y. G. Zhan, D. Ostrowski, M. Yellin, H. Marsh, A. M. Salazar, A. H. Rahman, B. D. Brown, M. Merad, J. D. Brody, *Nat. Med.* **2019**, *25*, 814; b) W. Ngamcherdrakul, M. Reda, M. A. Nelson, R. J. Wang, H. Y. Zaidan, D. S. Bejan, N. H. Hoang, R. S. Lane, S. W. Luoh, S. A. Leachman, G. B. Mills, J. W. Gray, A. W. Lund, W. Yantasee, *Adv. Mater.* **2021**, *33*, 2100628; c) J. J. Chen, M. Qiu, Z. F. Ye, T. Nyalile, Y. M. Li, Z. Glass, X. W. Zhao, L. Yang, J. Z. Chen, Q. B. Xu, *Sci. Adv.* **2021**, *7*, eabf1244.
- [4] a) T. Goto, *Vaccines* **2019**, *7*, 100; b) M. E. Rodriguez-Ruiz, I. Vitale, K. J. Harrington, I. Melero, L. Galluzzi, *Nat. Immunol.* **2020**, *21*, 120; c) K. Y. Ni, G. X. Lan, N. N. Guo, A. Culbert, T. K. Luo, T. Wu, R. R. Weichselbaum, W. B. Lin, *Sci. Adv.* **2020**, *6*, eabb5223.
- [5] a) E. Wennerberg, C. Lhuillier, C. Vanpouille-Box, K. A. Pilonas, E. Garcia-Martinez, N. P. Rudqvist, S. C. Formenti, S. Demaria, *Front. Immunol.* **2017**, *8*, 229; b) Y. Abuodeh, P. Venkat, S. Kim, *Curr. Probl. Cancer* **2016**, *40*, 25.
- [6] a) D. Sun, J. Zhang, L. Wang, Z. Yu, C. M. O'Driscoll, J. Guo, *Drug Discovery Today* **2021**, *26*, 651; b) L. Galluzzi, A. Buque, O. Kepp, L. Zitvogel, G. Kroemer, *Nat. Rev. Immunol.* **2017**, *17*, 97.
- [7] a) R. M. Chabanon, M. Rouanne, C. J. Lord, J. C. Soria, P. Pasero, S. Postel-Vinay, *Nat. Rev. Cancer* **2021**, *21*, 701; b) Y. X. Wang, Y. W. Ding, D. Yao, H. Dong, C. W. Ji, J. H. Wu, Y. Q. Hu, A. H. Yuan, *Small* **2021**, *17*, 2006231; c) C. Chen, X. Ni, S. Jia, Y. Liang, X. Wu, D. Kong, D. Ding, *Adv. Mater.* **2019**, *31*, 1904914; d) W. X. Zong, D. Ditsworth, D. E. Bauer, Z. Q. Wang, C. B. Thompson, *Genes Dev.* **2004**, *18*, 1272.
- [8] S. Bonvalot, P. L. Rutkowski, J. Thariat, *Lancet Oncol.* **2019**, *20*, 1148.
- [9] a) Y. Hu, S. Paris, H. Barsoumian, C. O. Abana, K. He, M. Wasley, A. I. Younes, F. Masrourpour, D. Chen, L. Yang, J. D. Dunn, J. Zhang, S. Gandhi, Q. N. Nguyen, M. A. Cortez, J. Welsh, *Int. J. Radiat. Oncol., Biol., Phys.* **2021**, *111*, 647; b) C. Shen, K. Jameson, J. Weiss, T. Hackman, D. Corum, J. A. Akulian, R. Dixon, A. Pearson, J. Frakes, P. Said, H. Miraoui, E. Baskin-Bey, T. Seiwert, *Ann. Oncol.* **2019**, *30*, xi46.
- [10] a) P. Jiang, W. J. Du, M. A. Wu, *Protein Cell* **2014**, *5*, 592; b) M. Li, X. X. He, W. X. Guo, H. M. Yu, S. C. Zhang, N. N. Wang, G. J. Liu, R. Sa, X. Shen, Y. B. Jiang, Y. F. Tang, Y. J. Zhuo, C. Z. Yin, Q. C. Tu, N. Li, X. Q. Nie, Y. Li, Z. M. Hu, H. W. Zhu, J. P. Ding, Z. Li, T. Liu, F. Zhang, H. Zhou, S. X. Li, J. Yue, Z. Yan, S. Q. Cheng, Y. Z. Tao, H. Y. Yin, *Nat. Cancer* **2020**, *1*, 735.
- [11] a) K. C. Patra, N. Hay, *Trends Biochem. Sci.* **2014**, *39*, 347; b) S. J. Moon, W. T. Dong, G. N. Stephanopoulos, H. D. Sikes, *Bioeng. Transl. Med.* **2020**, *5*, e10184.
- [12] X. Liu, K. Olszewski, Y. Zhang, E. W. Lim, J. Shi, X. Zhang, J. Zhang, H. Lee, P. Koppula, G. Lei, L. Zhuang, M. J. You, B. Fang, W. Li, C. M. Metallo, M. V. Poyurovsky, B. Gan, *Nat. Cell Biol.* **2020**, *22*, 476.
- [13] a) Y. Zhang, S. G. Martin, *Clin. Oncol.* **2014**, *26*, 289; b) N. S. Chandel, *Cold Spring Harbor Perspect. Biol.* **2021**, *13*, a040592.
- [14] a) H. Q. Ju, Y. X. Lu, Q. N. Wu, J. Liu, Z. L. Zeng, H. Y. Mo, Y. Chen, T. Tian, Y. Wang, T. B. Kang, D. Xie, M. S. Zeng, P. Huang, R. H. Xu, *Oncogene* **2017**, *36*, 6282; b) A. Kuehne, H. Emmert, J. Soehle, M. Winnefeld, F. Fischer, H. Wenck, S. Gallinat, L. Terstegen, R. Lucius, J. Hildebrand, N. Zamboni, *Mol. Cell* **2015**, *59*, 359; c) C. Riganti, E. Gazzano, M. Polimeni, E. Aldieri, D. Ghigo, *Free Radical Biol. Med.* **2012**, *53*, 421; d) R. L. Liu, W. F. Li, B. B. Tao, X. J. Wang, Z. Yang, Y. J. Zhang, C. Y. Wang, R. T. Liu, H. Gao, J. Liang, W. W. Yang, *Nat. Commun.* **2019**, *10*, 991; e) C.-L. Liu, Y.-C. Hsu, J.-J. Lee, M.-J. Chen, C.-H. Lin, S.-Y. Huang, S.-P. Cheng, *Mol. Cell. Endocrinol.* **2020**, *499*, 110595.
- [15] a) B. Rais, B. Comin, J. Puigjaner, J. L. Brandes, E. Creppy, D. Saboureau, R. Ennamany, W. N. P. Lee, L. G. Boros, M. Cascante, *FEBS Lett.* **1999**, *456*, 113; b) Q. Li, T. Qin, Z. Bi, H. Hong, L. Ding, J. Chen, W. Wu, X. Lin, W. Fu, F. Zheng, Y. Yao, M. L. Luo, P. E. Saw, G. M. Wulf, X. Xu, E. Song, H. Yao, H. Hu, *Nat. Commun.* **2020**, *11*, 1456; c) C. Cosentino, D. Grieco, V. Costanzo, *EMBO J.* **2011**, *30*, 546; d) K. Fornalewicz, A. Wieczorek, G. Wegrzyn, R. Lyzen, *Gene* **2017**, *635*, 33.
- [16] B. I. Lee, K. S. Lee, J. H. Lee, I. S. Lee, S. H. Byeon, *Dalton Trans.* **2009**, *14*, 2490.
- [17] Y. S. Yoon, B. I. Lee, K. S. Lee, G. H. Im, S. H. Byeon, J. H. Lee, I. S. Lee, *Adv. Funct. Mater.* **2009**, *19*, 3375.
- [18] a) R. Agarwal, P. Journey, M. Raythatha, V. Singh, S. V. Sreenivasan, L. Shi, K. Roy, *Adv. Healthcare Mater.* **2015**, *4*, 2269; b) B. W. Yang, Y. Chen, J. L. Shi, *Chem* **2018**, *4*, 1284.
- [19] a) C. S. Garris, J. J. Luke, *Clin. Cancer Res.* **2020**, *26*, 3901; b) A. R. Sanchez-Paulete, A. Teijeira, F. J. Cueto, S. Garasa, J. L. Perez-Gracia, A. Sanchez-Arrea, D. Sancho, I. Melero, *Ann. Oncol.* **2017**, *28*, xii74; c) M. Terranova-Barberio, N. Pawlowska, M. Dhawan, M. Moasser, A. J. Chien, M. E. Melisko, H. Rugo, R. Rahimi, T. Deal, A. Daud, M. D. Rosenblum, S. Thomas, P. N. Munster, *Nat. Commun.* **2020**, *11*, 3584.
- [20] a) H. Phuengkham, L. Ren, I. W. Shin, Y. T. Lim, *Adv. Mater.* **2019**, *31*, 1803322; b) M. Saxena, S. H. van der Burg, C. J. M. Melief, N. Bhardwaj, *Nat. Rev. Cancer* **2021**, *21*, 360.
- [21] a) X. Zhang, X. C. Bai, Z. J. Chen, *Immunity* **2020**, *53*, 43; b) E. C. Borden, *Nat. Rev. Drug Discovery* **2019**, *18*, 219; c) X. M. Yang,

- X. M. Zhang, M. L. Fu, R. R. Weichselbaum, T. F. Gajewski, Y. J. Guo, Y. X. Fu, *Cancer Cell* **2014**, *25*, 37.
- [22] K. Ni, G. Lan, C. Chan, B. Quigley, K. Lu, T. Aung, N. Guo, P. La Riviere, R. R. Weichselbaum, W. Lin, *Nat. Commun.* **2018**, *9*, 2351.
- [23] a) A. D. Yaprntsev, A. E. Baranchikov, V. K. Ivanov, *Russ. Chem. Rev.* **2020**, *89*, 629; b) J. Xu, X. Chen, Y. Xu, Y. Du, C. Yan, *Adv. Mater.* **2020**, *32*, 1806461.
- [24] a) L. J. McIntyre, L. K. Jackson, A. M. Fogg, *Chem. Mater.* **2008**, *20*, 335; b) F. X. Geng, Y. Matsushita, R. Z. Mat, H. Xin, M. Tanaka, F. Izumi, N. Iyi, T. Sasaki, *J. Am. Chem. Soc.* **2008**, *130*, 16344; c) F. Gandara, J. Perles, N. Snejko, M. Iglesias, B. Gomez-Lor, E. Gutierrez-Puebla, M. A. Monge, *Angew. Chem., Int. Ed.* **2006**, *45*, 7998.
- [25] a) C. H. Huang, K. Y. Chong, K. F. Lei, *ACS Appl. Mater. Interfaces* **2021**, *13*, 33885; b) H. Wang, H. Jiang, M. Van De Gucht, M. De Ridder, *Cancers* **2019**, *11*, 112.
- [26] a) B. Faubert, A. Solmonson, R. J. DeBerardinis, *Science* **2020**, *368*, 152; b) X. Li, P. Ramadori, D. Pfister, M. Seehawer, L. Zender, M. Heikenwalder, *Nat. Rev. Cancer* **2021**, *21*, 541; c) C. Wang, Z. Dong, Y. Hao, Y. Zhu, J. Ni, Q. Li, B. Liu, Y. Han, Z. Yang, J. Wan, K. Yang, Z. Liu, L. Feng, *Adv. Mater.* **2022**, *34*, 2106520.
- [27] a) E. Salas, S. Roy, T. Marsh, B. Rubin, J. Debnath, *Oncogene* **2016**, *35*, 2913; b) N. Bansal, J. Mims, J. G. Kuremsky, A. L. Olex, W. L. Zhao, L. M. Yin, R. Wani, J. Qian, B. Center, G. S. Marrs, M. Porosnicu, J. S. Fetrow, A. W. Tsang, C. M. Furdul, *Antioxid. Redox Signaling* **2014**, *21*, 221; c) I. Giacomini, E. Ragazzi, G. Pasut, M. Montopoli, *Int. J. Mol. Sci.* **2020**, *21*, 937; d) W. P. Hong, P. H. Cai, C. C. Xu, D. Cao, W. B. Yu, Z. X. Zhao, M. Huang, J. Jin, *Front. Pharmacol.* **2018**, *9*, 43; e) J. Mims, N. Bansal, M. S. Bharadwaj, X. Chen, A. J. Molina, A. W. Tsang, C. M. Furdul, *Radiat. Res.* **2015**, *183*, 291.
- [28] A. Kruger, N. M. Gruning, M. M. C. Wamelink, M. Kerick, A. Kirpy, D. Parkhomchuk, K. Bluemlein, M. R. Schweiger, A. Soldatov, H. Lehrach, C. Jakobs, M. Ralser, *Antioxid. Redox Signaling* **2011**, *15*, 311.
- [29] a) D. Christodoulou, H. Link, T. Fuhrer, K. Kochanowski, L. Gerosa, U. Sauer, *Cell Syst.* **2018**, *6*, 569; b) D. Christodoulou, A. Kuehne, A. Estermann, T. Fuhrer, P. Lang, U. Sauer, *iScience* **2019**, *19*, 1133.
- [30] a) V. M. Runge, *J. Magn. Reson. Imaging* **2000**, *12*, 205; b) R. T. Lin, S. Elf, C. L. Shan, H. B. Kang, Q. J. Ji, L. Zhou, T. Hitosugi, L. Zhang, S. Zhang, J. H. Seo, J. X. Xie, M. Tucker, T. L. Gu, J. Sudderth, L. Jiang, M. Mitsche, R. J. DeBerardinis, S. X. Wu, Y. C. Li, H. Mao, P. R. Chen, D. S. Wang, G. Z. Chen, S. J. Hurwitz, S. Lonial, M. L. Arellano, H. J. Khoury, F. R. Khuri, B. H. Lee, Q. Y. Lei, *Nat. Cell Biol.* **2015**, *17*, 1484.
- [31] C. C. Chien, H. Y. Wang, J. J. Wang, W. C. Kan, T. W. Chien, C. Y. Lin, S. B. Su, *Renal Failure* **2011**, *33*, 758.
- [32] Y. D. Xu, A. Goyanes, Y. W. Wang, A. J. Weston, P. W. So, C. F. G. C. Galdes, A. M. Fogg, A. W. Basit, G. R. Williams, *Dalton Trans.* **2018**, *47*, 3166.